Thrust at N³LL with Power Corrections and a Precision Global Fit for $\alpha_s(m_Z)$

Riccardo Abbate,[1] Michael Fickinger,[2] André H. Hoang,[3] Vicent Mateu,[3] and Iain W. Stewart[1]

[1]*Center for Theoretical Physics, Massachusetts Institute of Technology, Cambridge, MA 02139*
[2]*Department of Physics, University of Arizona, Tucson, AZ 85721*
[3]*Max-Planck-Institut für Physik (Werner-Heisenberg-Institut) Föhringer Ring 6, 80805 München, Germany*

We give a factorization formula for the e^+e^- thrust distribution $d\sigma/d\tau$ with $\tau = 1 - T$ based on soft-collinear effective theory. The result is applicable for all τ, i.e. in the peak, tail, and far-tail regions. The formula includes $\mathcal{O}(\alpha_s^3)$ fixed-order QCD results, resummation of singular partonic $\alpha_s^j \ln^k(\tau)/\tau$ terms with N³LL accuracy, hadronization effects from fitting a universal nonperturbative soft function defined in field theory, bottom quark mass effects, QED corrections, and the dominant top mass dependent terms from the axial anomaly. We do not rely on Monte Carlo generators to determine nonperturbative effects since they are not compatible with higher order perturbative analyses. Instead our treatment is based on fitting nonperturbative matrix elements in field theory, which are moments Ω_i of a nonperturbative soft function. We present a global analysis of all available thrust data measured at center-of-mass energies $Q = 35$ to 207 GeV in the tail region, where a two parameter fit to $\alpha_s(m_Z)$ and the first moment Ω_1 suffices. We use a short distance scheme to define Ω_1, called the R-gap scheme, thus ensuring that the perturbative $d\sigma/d\tau$ does not suffer from an $\mathcal{O}(\Lambda_{\rm QCD})$ renormalon ambiguity. We find $\alpha_s(m_Z) = 0.1135 \pm (0.0002)_{\rm expt} \pm (0.0005)_{\rm hadr} \pm (0.0009)_{\rm pert}$, with $\chi^2/{\rm dof} = 0.91$, where the displayed 1-sigma errors are the total experimental error, the hadronization uncertainty, and the perturbative theory uncertainty, respectively. The hadronization uncertainty in α_s is significantly decreased compared to earlier analyses by our two parameter fit, which determines $\Omega_1 = 0.323$ GeV with 16% uncertainty.

I. INTRODUCTION

A traditional method for testing the theory of strong interactions (QCD) at high-precision is the analysis of jet cross sections at e^+e^- colliders. Event shape distributions play a special role as they have been extensively measured with small experimental uncertainties at LEP and earlier e^+e^- colliders, and are theoretically clean and accessible to high-order perturbative computations. They have been frequently used to make precise determinations of the strong coupling α_s, see e.g. Ref. [1] for a review. One of the most frequently studied event shape variables is thrust [2],

$$T = \max_{\hat{\mathbf{t}}} \frac{\sum_i |\hat{\mathbf{t}} \cdot \vec{p}_i|}{\sum_i |\vec{p}_i|}, \qquad (1)$$

where the sum i is over all final-state hadrons with momenta $\vec{p}_i$. The unit vector $\hat{\mathbf{t}}$ that maximizes the right-hand side (RHS) of Eq. (1) defines the thrust axis. We will use the more convenient variable $\tau = 1 - T$. For the production of a pair of massless quarks at tree level $d\sigma/d\tau \propto \delta(\tau)$, so the measured distribution for $\tau > 0$ involves gluon radiation and is sensitive to the value of α_s. The thrust value of an event measures how much it resembles two jets. For τ values close to zero the event has two narrow, pencil-like, back-to-back jets, carrying about half the center-of-mass (c.m.) energy into each of the two hemispheres defined by the plane orthogonal to $\hat{\mathbf{t}}$. For τ close to the multijet endpoint $1/2$, the event has an isotropic multi-particle final state containing a large number of low-energy jets.

On the theoretical side, for $\tau < 1/3$ the dynamics is governed by three different scales. The *hard scale* $\mu_H \simeq Q$ is set by the e^+e^- c.m. energy Q. The *jet scale, $\mu_J \simeq Q\sqrt{\tau}$* is the typical momentum transverse to $\hat{\mathbf{t}}$ of the particles within each of the two hemispheres, or the jet invariant mass scale if all energetic particles in a hemisphere are grouped into a jet. There is also uniform soft radiation with energy $\mu_S \simeq Q\tau$, called the *soft scale*. The physical description of the thrust distribution can be divided into three regions,

$$
\begin{array}{lll}
\text{peak region:} & \tau \sim 2\Lambda_{\rm QCD}/Q\,, & \\
\text{tail region:} & 2\Lambda_{\rm QCD}/Q \ll \tau \lesssim 1/3\,, & (2) \\
\text{far-tail region:} & 1/3 \lesssim \tau \leq 1/2\,. &
\end{array}
$$

In the *peak region* the hard, jet, and soft scales are Q, $\sqrt{Q\Lambda_{\rm QCD}}$, and $\Lambda_{\rm QCD}$, and the distribution shows a strongly peaked maximum. Theoretically, since $\tau \ll 1$ one needs to sum large (double) logarithms, $(\alpha_s^j \ln^k \tau)/\tau$, and account for the fact that $\mu_S \simeq \Lambda_{\rm QCD}$, so $d\sigma/d\tau$ is affected at leading order by a nonperturbative distribution. We call this distribution the nonperturbative soft function. The *tail region* is populated predominantly by broader dijets and 3-jet events. Here the three scales are still well separated and one still needs to sum logarithms, but now $\mu_S \gg \Lambda_{\rm QCD}$, so soft radiation can be described by perturbation theory and a series of power correction parameters Ω_i. Finally, the *far-tail* region is populated by multijet events. Here the distinction of the three scales becomes meaningless, and accurate predictions can be made with fixed-order perturbation theory supplemented with power corrections. The transition

	sum logs	power corrections	$\alpha_s(m_Z)$
Ref. [22]	no	Monte Carlo (MC)	$0.1240 \pm 0.0034^*$
Ref. [20]	N^{3}LL	uncertainty from MC	$0.1172 \pm 0.0021^*$
Ref. [23]	NLL	effective coupling model	$0.1164 \pm 0.0028^\#$
Ref. [24]	NLL	Monte Carlo	$0.1172 \pm 0.0051^{**}$
Ref. [25]	NLL	Monte Carlo	$0.1224 \pm 0.0039^*$

TABLE I: Recent thrust analyses which use the $\mathcal{O}(\alpha_s^3)$ fixed-order results. The theoretical component of the errors were determined as indicated, by either: * the error band method, ** variation of the renormalization scale μ, or # by a simultaneous fit to $\alpha_s(m_Z)$ and α_0 (see text for more details). The analyses of Refs. [20, 23] used thrust data only, while Refs.[22, 24, 25] employed six different event shapes.

to this region must be handled carefully since including a summation of $(\alpha_s^j \ln^k \tau)/\tau$ terms in this region spoils the cancellations that take place at fixed order multijet thresholds, and hence would induce uncertainties that are significantly larger than those of the fixed-order results.

Recently two very important achievements were made improving the theoretical description of event shape distributions in e^+e^- annihilation. First, in the work of Gehrmann et al. in Refs. [3, 4] and Weinzierl in Refs. [5, 6] the full set of $\mathcal{O}(\alpha_s^3)$ contributions to the 2-, 3- and 4-jet final states were determined. These results were made available in the program package EERAD3 [3]. Second, soft-collinear effective theory (SCET) [7, 8, 9, 10, 11] provides a systematic framework to treat nonperturbative corrections [12, 13] and to factorize and compute hard, collinear and soft contributions for jet production to all orders in α_s [14, 15, 16], building on earlier all orders QCD factorization results [17, 18, 19]. The SCET framework allows for the summation of large logarithms at higher orders, as demonstrated by the analytic calculation of the thrust distribution at N^{3}LL order by Becher and Schwartz in Ref. [20].[1] In contrast, the classic exponentiation techniques of Ref. [21] for event shapes have so far only been carried out to NLL order. Also, the anomalous dimensions in SCET relevant for thrust are valid over perturbative momentum scales, and there are no Landau pole ambiguities in the resummation at any order. In addition, as we will discuss in the body of our paper, SCET provides a rigorous framework for including perturbative and nonperturbative contributions, which can be used to connect power corrections in factorization theorems to those in an operator expansion for thrust moments. Moreover it provides a simple method to simultaneously treat the peak, tail, and far-tail regions.

Several determinations of α_s in the tail region have been carried out incorporating the fixed-order $\mathcal{O}(\alpha_s^3)$ re-

sults, which we have collected in Tab. I. They differ on which event shape data has been used for the fits, on the accuracy of the partonic resummation of logarithms in the theory formula, the approach for nonperturbative hadronization effects, and how the theory errors are estimated. It is instructive to compare the analyses by Dissertori et al. [22, 25] and by Becher and Schwartz [20], which both used the error band method [26] to determine theoretical uncertainties. The improved convergence and reduced theoretical uncertainty for $\alpha_s(m_Z)$ obtained by Becher and Schwartz indicates that the summation of logarithms beyond NLL order level is important. Both the analyses by Dissertori et al. and Becher and Schwartz are limited by the fact that they used Monte Carlo (MC) generators to estimate the size of nonperturbative corrections.

The use of e^+e^- MC generators to estimate power corrections is problematic since the partonic contributions are based on LL parton showers with at most one-loop matrix elements, complemented by hadronization models below the shower cutoff that are not derived from QCD. The parameters of these models have been tuned to LEP data, and thus unavoidably encode both nonperturbative effects as well as higher order perturbative corrections. Hence, one must worry about double counting, and this makes MC generators unreliable for estimating nonperturbative corrections in higher order LEP analyses. Moreover, purely perturbative results for event shapes in the $\overline{\text{MS}}$ scheme such as those in Refs. [6, 20, 22, 25] suffer from infrared effects known as infrared renormalons (see Ref. [27] for a review of the early literature). These infrared effects arise because fluctuations from large angle soft radiation down to arbitrarily small momenta are included in the $\overline{\text{MS}}$ perturbative series and can cause unphysical large corrections already in low-order perturbative QCD results. On the other hand, the hard shower cutoff protects the parton level MC from infrared renormalons. Hence one cannot rigorously combine MC hadronization effects with strict perturbative $\overline{\text{MS}}$ results. From the two points raised above, we conclude that the $\alpha_s(m_Z)$ results obtained in Refs. [20, 22, 25] contain a systematic theoretical error from nonperturbative effects that can be quite sizeable. We emphasize that this criticism also applies in part to the numerous earlier event shape analyses which estimated nonperturbative corrections using MC generators, see Ref. [1] for a review.

The presence of $\Lambda_{\text{QCD}}/(Q\tau)$ power corrections in $d\sigma/d\tau$ have been discussed in earlier literature [28, 29, 30, 31, 32, 33, 34], where it has been argued that the leading effect is a shift in the thrust distribution, $\tau \to \tau - 2\Lambda/Q$ with $\Lambda \sim \Lambda_{\text{QCD}}$. The analyses with the $\mathcal{O}(\alpha_s^3)$ results, that discuss nonperturbative effects in the thrust tail region without relying on MC generators are: Ref. [20] which examined a $1/Q$ power correction in a simple soft function model, but due to the large induced uncertainty on $\alpha_s(m_Z)$ does not use it for their final error analysis, and Ref. [23] which uses the effective coupling model.

For the most accurate data at $Q = m_Z$ the change to

---

[1] The calculation of Ref. [20] also revealed a numerical problem at small τ in the initial fixed-order results of Refs. [3, 4].
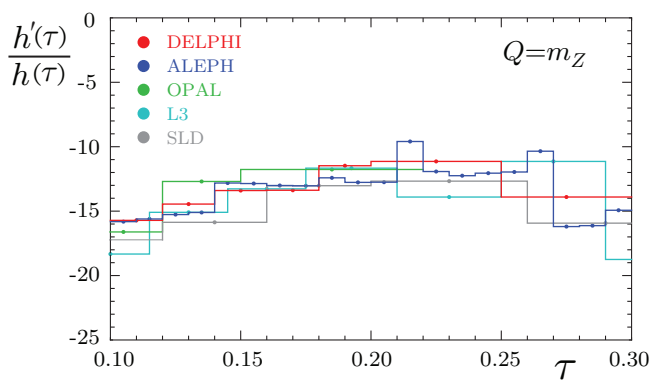
FIG. 1: Plot of $h'(\tau)/h(\tau)$, the slope of $\ln[(1/\tau)\mathrm{d}\sigma/\mathrm{d}\tau]$, computed from experimental data at $Q = m_Z$. The derivative is computed using the central difference with neighboring experimental bins.

the extracted $\alpha_s(m_Z)$ from including the leading power correction can be quite significant, at the 10% level. We can derive this estimate by a simple calculation. We first write the cross section with a shift due to the power correction, $(1/\sigma)\mathrm{d}\sigma/\mathrm{d}\tau = h(\tau - 2\Lambda/Q)$. Assuming h is proportional to α_s, and expanding for $\Lambda/Q \ll 1$, one can easily derive that the change in the α_s value extracted from data due to the existence of the power correction is

$$\frac{\delta\alpha_s}{\alpha_s} \simeq \frac{2\Lambda}{Q} \frac{h'(\tau)}{h(\tau)}. \tag{3}$$

The expression in Eq. (3) gives a scaling estimate for the fractional change in α_s from an analysis with the power correction compared to one without, using data at τ. To the extent that the assumptions stated above are realized, the slope factor $h'(\tau)/h(\tau)$ should be constant. In Fig. 1 we show the slope factor computed from experimental data at $Q = m_Z$. The figure shows that the slope factor is indeed only weakly depending on τ in the tail region and we get $h'(\tau)/h(\tau) \simeq -14 \pm 4$. The remaining visible variation in τ is related to subleading nonperturbative and higher power α_s effects that are not accounted for in our simple scaling estimate. For a QCD power correction of natural size, $\Lambda = 0.3\,\mathrm{GeV}$, Eq. (3) gives $\delta\alpha_s/\alpha_s \simeq -(9 \pm 3)\%$ for $Q = m_Z$. The magnitude of this effect makes it important to treat power corrections as accurately as possible in a fit to thrust data. We will show in later sections of this work that the relative downward shift in the fitted $\alpha_s(m_Z)$ due to nonperturbative effects is indeed at the level of the scaling estimate of -10%.

In the $\mathrm{NLL}/\mathcal{O}(\alpha_s^3)$ analysis by Davison and Webber [23] the nonperturbative effects are incorporated through a power correction α_0 which is fit together with α_s to the experimental data. The power correction is formulated from the low-scale effective coupling model of Ref. [35], which modifies $\alpha_s(\mu)$ below $\mu = \mu_I = 2\,\mathrm{GeV}$, and defines α_0 as the average value of the coupling between $\mu = 0$ and μ_I. It is important that the effective

coupling model correctly predicts the Q dependence of the leading nonperturbative power correction in factorization [18, 35]. This model also induces a subtraction of perturbative contributions below the momentum cutoff μ_I (based on the running coupling approximation) and thus removes infrared renormalon ambiguities.[2] However the model is not based on factorization, and hence this treatment of nonperturbative corrections is not systematically improvable. It is therefore not easy to judge the corresponding uncertainty. Another problem of the effective coupling model is that its subtractions involve large logs, $\ln(\mu_I/Q)$, which are not resummed. This effects the Q dependence in the interplay between perturbative and nonperturbative effects.

In this paper we extend the event shape formalism to resolve the theoretical difficulties mentioned above. Our results are formulated in the SCET framework, and hence are rigorous predictions of QCD. The formula we derive has a $\mathrm{N}^3\mathrm{LL}$ order summation of logarithms for the partonic singular $\alpha_s^j \ln^k(\tau)/\tau$ terms, and $\mathcal{O}(\alpha_s^3)$ fixed-order contributions for the partonic nonsingular terms. Our theoretical improvements beyond earlier work include:

- A factorization formula that can be simultaneously applied to data in the peak and the tail regions of the thrust distribution and for multiple c.m. energies Q, as well as being consistent with the multijet thresholds in the far-tail region.

- In the factorization formula a nonperturbative soft function defined from field theory is implemented using the method of Ref. [16] to incorporate hadronization effects. To achieve independence of a particular analytic ansatz in the peak region, the nonperturbative part of the soft function uses a linear combination of orthogonal basis functions that converge quickly for confined functions [38].

- In the tail region the leading power correction to $\mathrm{d}\sigma/\mathrm{d}\tau$ is determined by a nonperturbative parameter Ω_1 that appears through a factorization theorem for the singular distribution. Ω_1 is a field theory matrix element of an operator, and is also related to the first moment of the nonperturbative soft function. In the tail region the effects of Ω_1 hadronization corrections are included for the nonsingular corrections that are kinematically subleading in the dijet limit, based on theoretical consistency with the far-tail region.

- Defining the matrix element $\bar{\Omega}_1$ in $\overline{\mathrm{MS}}$, the perturbative cross section suffer from an $\mathcal{O}(\Lambda_{\mathrm{QCD}})$ renor-

---

[2] Another thrust analysis where infrared renormalon contributions have been removed from the partonic contributions is by Gardi and Rathsman in Refs. [36, 37], which used a principal value prescription for the inverse Borel transformation of the thrust distribution. Their analysis was prior to the new $\mathcal{O}(\alpha_s^3)$ fixed-order computations, and hence was not included in Table I.

malon. In our analysis this renormalon is removed by using an R-gap scheme for the definition of Ω_1 [16]. This scheme choice induces subtractions on the leading power $\overline{\text{MS}}$ cross section which simultaneously remove the renormalon there. Large logarithms in the subtractions are summed to all orders in α_s using R-evolution equations given in Refs. [39, 40].

- Finite bottom quark mass corrections are included using a factorization theorem for event shapes involving massive quarks, derived in Refs. [14, 41].

- QED corrections at NNLL order are incorporated, counting $\alpha_{\text{em}} \sim \alpha_s^2$. This includes QED Sudakov effects, final state radiation, and QED/QCD renormalization group interference.

- The 3-loop finite term h_3 of the quark form factor in $\overline{\text{MS}}$ is extracted using the results of Ref. [42], and is included in our analysis.

- The most important corrections from the axial anomaly are included. The anomaly modifies the axial-vector current contributions at $\mathcal{O}(\alpha_s^2)$ by terms involving the top quark mass.

Electroweak effects from virtual W and Z loops mostly effect the normalization of the cross section and so their dominant contribution drops out of $(1/\sigma)\mathrm{d}\sigma/\mathrm{d}\tau$ [43, 44]. These corrections are not included in our analysis.

For the numerical analyses carried out in this work we have created within our collaboration two completely independent codes. One code within Mathematica [45] implements the theoretical expressions exactly as given in this paper, and one code is based on theoretical formulae in Fourier space and realized as a fast Fortran code suitable for parallelized runs on computer clusters. These two codes agree for the thrust distribution at the level of 10^{-6}.

While the resulting theoretical code can be used for all values of τ, in this paper we focus our numerical analysis on a global fit of e^+e^- thrust data in the tail region, for c.m. energies Q between 35 and 207 GeV, to determine $\alpha_s(m_Z)$.[3] Our global fit exhibits consistency across all available data sets, and reduces the overall experimental uncertainty. For a single Q we find a strong correlation between the effect of $\alpha_s(m_Z)$ and Ω_1 on the cross section. This degeneracy is broken by fitting data at multiple Qs. The hadronization uncertainty is significantly decreased by our simultaneous global fit to $\alpha_s(m_Z)$ and Ω_1. To estimate the perturbative uncertainty in the fit we use a random scan in a 12-dimensional theory parameter space. This space includes 6 parameters for μ-variation, 3 parameters for theory uncertainties related to the finite

---

[3] Throughout this paper we use the $\overline{\text{MS}}$ scheme for α_s with five light flavors.

statistics of the numerical fixed-order results, one parameter for the unknown 4-loop cusp anomalous dimension, and two parameters for unknown constants in the perturbative 3-loop jet and 3-loop soft functions. The scan yields a more conservative theory error than the error band method [26]. Despite this we are able to achieve smaller perturbative uncertainties than earlier analyses due to our removal of the $\mathcal{O}(\Lambda_{\text{QCD}})$ renormalon and the inclusion of h_3. We also analyze in detail the dependence of the fit results on the range in τ used in the fit.

The outline of the paper is as follows. In Sec. II we introduce the theoretical framework and discuss the various theoretical ingredients in our final $\mathrm{d}\sigma/\mathrm{d}\tau$ formula. In Sec. III we present the profile functions which allow us to simultaneously treat multiple τ regions, and discuss the 6 parameters used for μ-variation in the analysis of the perturbative uncertainty. In Sec. IV we review the parametrization of the nonperturbative function. In Sec. V we discuss the normalization of our distributions and compare results at different orders in perturbation theory for: fixed-order results, adding the log resummation, adding the nonperturbative corrections, and adding the renormalon subtractions. In Sec. VI we discuss the experimental data and the fit procedure. Our results for $\alpha_s(m_Z)$ and the soft function moment Ω_1 from the global fit are presented in Sec. VII, including a discussion of the theory errors. In Sec. VIII we use our tail fit results to make predictions in the far-tail and peak regions, and compare with data. Cross checks on our code are discussed in Sec. IX, including using it to reproduce the earlier lower precision fits of Dissertori et al. [22] and Becher and Schwartz [20]. Section X contains our conclusions and outlook, including prospects for future improvements based on the universality of the parameter Ω_1. The analytic theoretical expressions that went into our analysis for massless quarks and QCD effects are presented in condensed form in Appendix A. In Appendix B we use the operator product expansion for the soft function in the tail region, discussing uniqueness and deriving an all order relation for the Wilson coefficient of Ω_1. In Appendix C we use an OPE for the first moment of the thrust distribution to show that it involves the same Ω_1 at lowest order. Readers most interested in our numerical results can skip directly to Sections VI and VII.

II. FORMALISM

A. Overview

The factorization formula we use for the fits to the experimental thrust data is

$$
\begin{aligned}
\frac{\mathrm{d}\sigma}{\mathrm{d}\tau} = \int \mathrm{d}k \left(\frac{\mathrm{d}\hat{\sigma}_s}{\mathrm{d}\tau} + \frac{\mathrm{d}\hat{\sigma}_{\text{ns}}}{\mathrm{d}\tau} + \frac{\Delta \mathrm{d}\hat{\sigma}_b}{\mathrm{d}\tau} \right) \left(\tau - \frac{k}{Q} \right) \\
\times S_\tau^{\text{mod}}\left(k - 2\bar{\Delta}(R, \mu_S) \right) + \mathcal{O}\left(\sigma_0\, \alpha_s \frac{\Lambda_{\text{QCD}}}{Q} \right).
\end{aligned} \quad (4)
$$

Here $d\hat{\sigma}_s/d\tau$ contains the singular partonic QCD corrections $\alpha_s^j [\ln^k(\tau)/\tau]_+$ and $\alpha_s^j \delta(\tau)$ with the standard plus-functions as defined in Eq. (A17). It also contains the singular partonic QED corrections depending on $\alpha_{\rm em}$ which are discussed in Sec. II H. This $d\hat{\sigma}_s/d\tau$ term accounts for matrix element corrections and the resummation of $\ln\tau$ terms within the SCET formalism up to N³LL order, which we discuss in Sec. II C. Our definition of N³LL, N³LL′, and other orders is discussed in detail in Sec. II B (see also Tab. II).

The term $d\hat{\sigma}_{\rm ns}/d\tau$, which we call the nonsingular partonic distribution, contains the thrust distribution in strict fixed-order expansion with the singular terms $\propto \alpha_s^j \ln^k(\tau)/\tau$ subtracted to avoid double counting. The most singular terms in $d\hat{\sigma}_{\rm ns}/d\tau$ scale as $\ln^k\tau$ for $\tau \to 0$.[4] Our implementation of nonsingular terms is discussed in detail in Sec. II E.

Finally, $\Delta d\hat{\sigma}_b/d\tau$ contains corrections to the singular and nonsingular cross sections due to the finite mass of the bottom quark. The b-mass corrections are implemented as a difference of the massive and massless cross sections computed at NNLL order as discussed in Sec. II G.

The function $S_\tau^{\rm mod}$ that is convoluted with these partonic cross sections in Eq. (4) describes the nonperturbative effects from soft gluons including large angle soft radiation [18, 46]. The definition of $S_\tau^{\rm mod}$ also depends on the hemisphere prescription inherent to the thrust variable. This is a hadronic function that enters in a universal way for both massless and massive cross sections, and is independent of the value of Q. The universality of $S_\tau^{\rm mod}$ in Eq. (4) follows from the leading power thrust factorization theorem [14, 15, 18], and the thrust factorization theorem for massive quarks in Refs. [14, 41]. Our treatment of the convolution of $S_\tau^{\rm mod}$ with $d\hat{\sigma}_{\rm ns}/d\tau$ yields a consistent treatment of multijet thresholds and the leading power correction to the operator expansion for the first moment of thrust. Details of our implementation of power corrections and nonperturbative corrections are discussed in Sec. II D and Sec IV. The function $S_\tau^{\rm mod}$ is normalized to unity and can be determined from experimental data. Its form depends on a gap parameter $\bar{\Delta}$ and additional moment parameters Ω_i which are discussed below.

The factorization formula given in Eq. (4) can be applied simultaneously in the peak, tail, and the far-tail regions of Eq. (2), i.e. for all τ values. In the peak region $d\hat{\sigma}_{\rm ns}/d\tau$ is significantly smaller than $d\hat{\sigma}_s/d\tau$, and the full analytic form of the soft nonperturbative function $S_\tau^{\rm mod}(k)$ is relevant to determine the τ-distribution since $\mu_S \simeq \Lambda_{\rm QCD}$. Because $\mu_H \gg \mu_J \gg \mu_S$, the summation of logarithms of τ is also crucial to achieve an accurate theoretical description.

For much of the tail region the summation of $\ln\tau$ terms remains important, although this is no longer the case when we reach $\tau \simeq 1/3$. Likewise, the dominance of the singular partonic contributions remains as long as $\tau < 1/3$, but the nonsingular terms become more important for increasing τ (see Fig. 7 below). Near $\tau \simeq 1/3$ the nonsingular terms become equal in size to the singular terms with opposite sign. Since $\mu_S \gg \Lambda_{\rm QCD}$ in the tail region the effects of $S_\tau^{\rm mod}$ can be parameterized in terms of the moments

$$\Omega_i = \int dk \left(\frac{k}{2}\right)^i S_\tau^{\rm mod}(k - 2\bar{\Delta}), \qquad (5)$$

where $\Omega_0 = 1$ since $S_\tau^{\rm mod}$ is normalized. Their importance is determined by $\Omega_i/(Q\tau)^i$ as discussed in Sec. II D, so the first moment Ω_1 parameterizes the dominant power correction and higher moments provide increasingly smaller corrections. The first moment is defined by

$$\Omega_1 \equiv \bar{\Delta} + \frac{1}{2N_c}\langle 0|{\rm tr}\,\overline{Y}_{\bar{n}}^T(0)Y_n(0)\,i\widehat{\partial}\,Y_n^\dagger(0)\overline{Y}_{\bar{n}}^*(0)|0\rangle, \quad (6)$$

where $Y_n^\dagger(0) = {\rm P}\exp\left(ig\int_0^\infty ds\,n\cdot A(ns)\right)$, $\overline{Y}_{\bar{n}}^\dagger$ is similar but in the $\overline{3}$ representation, and we trace over color. Here

$$i\widehat{\partial} \equiv \theta(i\bar{n}\cdot\partial - in\cdot\partial)\,in\cdot\partial + \theta(in\cdot\partial - i\bar{n}\cdot\partial)\,i\bar{n}\cdot\partial, \quad (7)$$

is a derivative operator[5] involving light-like vectors $n = (1,\hat{\mathbf{t}})$ and $\bar{n} = (1,-\hat{\mathbf{t}})$. Ω_1 is the field theory analog of the parameter α_0 employed in the low-scale effective coupling approach to power corrections. Since the renormalon subtractions depend on a cutoff scale R and the renormalization scale μ_S, all moments $\Omega_i(R,\mu_S)$ as well as $\bar{\Delta}(R,\mu_S)$ are scale and scheme dependent quantities. The scheme we use to define $\Omega_1(R,\mu_S)$ is described in Sec. II F. In our fit to experimental data we use the R-gap scheme, and extract the first moment at a reference scale $R_\Delta = \mu_\Delta = 2$ GeV, i.e. we use $\bar{\Delta}(R_\Delta,\mu_\Delta)$ and hence $\Omega_1 = \Omega_1(R_\Delta,\mu_\Delta)$. In the factorization theorem the gap appears evaluated at $\bar{\Delta}(R,\mu_S)$ and the scales (R,μ_S) are connected to the reference scales (R_Δ,μ_Δ) using renormalization group equations.

Finally, in the far-tail region $\tau \simeq 0.3$ the singular and the nonsingular partonic contributions $d\hat{\sigma}_s/d\tau$ and $d\hat{\sigma}_{\rm ns}/d\tau$ become nearly equal with opposite signs, exhibiting a strong cancellation. This is due to the strong suppression of the fixed-order distribution in the three- and four-jet endpoint regions at $\tau \gtrsim 1/3$ in fixed-order perturbation theory. In this region the summation of logarithms of τ must be switched off to avoid

---

[4] For $d\hat{\sigma}_{\rm ns}/d\tau$ the resummation of $\ln\tau$ terms is currently unknown. These terms could be determined with subleading factorization theorems in SCET.

[5] Note that $i\widehat{\partial}$ is defined in the c.m. frame of the colliding e^+e^-. One may also write $i\widehat{\partial} = \int d\eta\, e^{-|\eta|}\hat{\mathcal{E}}_T(\eta)$ where $\hat{\mathcal{E}}_T(\eta)$ measures the sum of absolute transverse momenta at a given rapidity η with respect to the thrust axis $\hat{t}$ [18, 47].

messing up this cancellation. Here our Eq. (4) reduces to the pure fixed-order partonic thrust distribution supplemented with power corrections coming from the convolution with the soft function. All three regions are smoothly joined together in Eq. (4). The proper summation (or non-summation) of logarithms is achieved through τ-dependent renormalization scales, $\mu_J(\tau)$, $\mu_S(\tau)$, and $R(\tau)$ which we call *profile functions*. They are discussed in detail in Sec. III.

In the following subsections various ingredients of the factorization formula of Eq. (4) are presented in more detail. Compact results for the corresponding analytic expressions for massless quarks in QCD are given in App. A. In Secs. II G and II H we describe how finite bottom mass and QED corrections are included in our analysis. The full formulae for these corrections will be presented in a future publication.

B. Order Counting

In the classic order counting used for fits to event shape distributions it is common to separately quote orders for the summation of logarithms and the fixed-order matching contributions. For fixed-order contributions the $\mathcal{O}(\alpha_s)$ contributions are called LO, the $\mathcal{O}(\alpha_s^2)$ contributions are called NLO, etc. This counting is motivated from the fact that at tree level the fixed-order thrust distribution vanishes for $\tau > 0$. For the summation one refers to LL (leading-log) summation if the one-loop cusp anomalous dimension is used to sum the double Sudakov logs, and NLL (next-to-leading-log) if the two-loop cusp and the one-loop non-cusp anomalous dimension terms are also included.

In our analysis the summation orders (LL, NLL, ...) match the classical language. For the fixed-order contributions we account for the tree level $\delta(\tau)$ in LL and NLL, and we include $\mathcal{O}(\alpha_s)$ corrections at NLL′ and NNLL, etc, as shown in Tab. IIa. In SCET the summation can be carried out at both NNLL and N³LL [20]. The corresponding loop orders for the anomalous dimensions are also shown in Tab. IIa. Within SCET the summation of logarithms is achieved by renormalization group evolution and the fixed-order corrections enter as series evaluated at each of the transition scales μ_H, μ_J, and μ_S which we refer to as matching or matrix element corrections. The logs in the singular thrust cross section exponentiate to all orders if we use y, the Fourier-transformed variable to τ. The orders we consider correspond to summing the terms

$$\ln\left[\frac{d\tilde{\sigma}_s}{dy}\right] \sim \left[L\sum_{k=1}^{\infty}(\alpha_s L)^k\right]_{\mathrm{LL}} + \left[\sum_{k=1}^{\infty}(\alpha_s L)^k\right]_{\mathrm{NLL}} \qquad (8)$$

$$+ \left[\alpha_s\sum_{k=0}^{\infty}(\alpha_s L)^k\right]_{\mathrm{NNLL}} + \left[\alpha_s^2\sum_{k=0}^{\infty}(\alpha_s L)^k\right]_{\mathrm{N^3LL}},$$

where $L = \ln(iy)$, and the series in the exponent makes

clear the structure of the large logs that are summed at each order.

The nonsingular counting in Tab. IIa for the fixed-order series in $d\hat{\sigma}_{\mathrm{ns}}/d\tau$ must be the same as for the matching and matrix element corrections to ensure that we exactly reproduce the fixed-order cross section when the resummed result is expanded. Since the relative importance of the log resummation and the nonsingular terms varies depending on the τ-region, we also consider an alternative "primed" counting scheme. In the primed counting all series for fixed-order quantities are included to one higher order in α_s. In this counting scheme the $\mathcal{O}(\alpha_s^3)$ fixed-order results occur in N³LL′, which is the order we use for our final analysis.

Also shown in Tab. IIa are columns for the fixed-order gap subtractions $\delta = \delta(R, \mu)$, and the gap anomalous dimensions $\gamma_{\Delta}^{\mu,R}$. These terms are required to remove the leading $\mathcal{O}(\Lambda_{\mathrm{QCD}})$ renormalon from the perturbative corrections, while still maintaining the same level of log resummation for terms in the cross section. The resummation of these large logarithms is missing in the recent analysis of Ref. [23] and is discussed further in Sec. II F.

A crucial aspect of our analysis is the inclusion of power corrections in a rigorous manner through field theoretic techniques. In the effective theory there are several types of power corrections which arise from the possible ratios of the scales μ_H, μ_J, μ_S, and Λ_{QCD}:

$$1) \quad \frac{\Lambda_{\mathrm{QCD}}}{\mu_S} = \frac{\Lambda_{\mathrm{QCD}}}{Q\tau},$$

$$2) \quad \frac{\mu_S^2}{\mu_J^2} = \tau,$$

$$3) \quad \frac{\Lambda_{\mathrm{QCD}}}{\mu_H} = \frac{\Lambda_{\mathrm{QCD}}}{Q}. \qquad (9)$$

Any $\Lambda_{\mathrm{QCD}}/\mu_J$ power correction can be taken as a cross-term between types 1) and 2) for the purpose of enumeration. The type 1 power corrections are enhanced by the presence of the soft scale and are encoded by the moments $\Omega_k \sim \Lambda_{\mathrm{QCD}}^k$ of the soft function. Type 2 are kinematic power corrections that occur because of the expansion about small τ, and can be computed with perturbation theory. The importance of these first two types depends on the region considered in Eq. (2), with all terms in type 2 becoming leading order for the far-tail region. Type 3 are non-enhanced power correction that are of the same size in any region. There are also cross-terms between the three types.

In our analysis we keep all power corrections of types 1 and 2, and the dominant terms of type 3. Our treatment of the nonsingular cross section also includes cross-terms between 1 and 2 in a manner that is discussed in Sec. II D. For the different thrust regions we display the relevant terms kept in our analysis in Tab. IIb. The nonsingular cross section corrections fully account for the power corrections of type 2. The factor $[\Lambda_{\mathrm{QCD}}/(Q\tau)]^k$ in the peak region denotes the fact that we sum over all type 1 power corrections from the leading soft function. In the

a) Perturbative Corrections

	cusp	non-cusp	matching	$\beta[\alpha_s]$	nonsingular	$\gamma^{\mu,R}_\Delta$	δ
LL	1	-	tree	1	-	-	-
NLL	2	1	tree	2	-	1	-
NNLL	3	2	1	3	1	2	1
N³LL	4$^{\text{pade}}$	3	2	4	2	3	2
NLL'	2	1	1	2	1	1	1
NNLL'	3	2	2	3	2	2	2
N³LL'	4$^{\text{pade}}$	3	3	4	3	3	3

b) Nonperturbative Corrections with $\Omega_k \sim \Lambda^k_{\text{QCD}}$

	peak (any k)	tail and far-tail ($k = 0, 1, 2$)
$\dfrac{\mathrm{d}\hat\sigma_s}{\mathrm{d}\tau}$	$\alpha_s^i \, \dfrac{\ln^j\tau}{\tau} \, \dfrac{\Omega_k}{(Q\tau)^k}$	$\alpha_s^i \, \dfrac{\ln^j\tau}{\tau} \, \dfrac{\Omega_k}{(Q\tau)^k}$
$\dfrac{\mathrm{d}\hat\sigma_{n_s}}{\mathrm{d}\tau}$	$\alpha_s^i \, f_{ik}(\tau) \dfrac{\Omega_k}{(Q\tau)^k}$	$\alpha_s^i \, f_{ik}(\tau) \dfrac{\Omega_k}{(Q\tau)^k}$
$\dfrac{\mathrm{d}\hat\sigma_b}{\mathrm{d}\tau}$	$\alpha_s^i \, g_{ik}\left(\tau, \tfrac{m_b}{Q}\right) \dfrac{\Omega_k}{(Q\tau)^k}$	$\alpha_s^i \, g_{ik}\left(\tau, \tfrac{m_b}{Q}\right) \dfrac{\Omega_k}{(Q\tau)^k}$
p.c.	$\alpha_s \dfrac{\Lambda_{\text{QCD}}}{Q}$	$\alpha_s \dfrac{\Lambda_{\text{QCD}}}{Q}$

TABLE II: Perturbative and nonperturbative corrections included in our analysis. a) (left panel) Loop orders j for perturbative corrections of $\mathcal{O}(\alpha_s^j)$. Here cusp, non-cusp, and $\gamma^{\mu,R}_\Delta$ refer to anomalous dimensions, while matching, nonsingular, and the gap subtraction δ refer to fixed-order series. For convenience in our numerical analysis we use the four-loop beta function for the α_s running in all orders displayed. b) (right panel) Nonperturbative corrections included in $\mathrm{d}\sigma/\mathrm{d}\tau$ with implicit sums over i and k. All powers $\Omega_k/(Q\tau)^k$ can be included in the peak region with the function S_τ^{mod}, while only a fixed set of power correction parameters are included in the tail and far-tail regions. The row labeled p.c. shows the scaling of the the first power correction that is not entirely determined by the earlier rows and hence yield corrections to Eq. (4).

tail and multijet regions we only consider the first three orders: k=0 (partonic result), k=1 (power correction involving Ω_1) and , k=2 (power correction involving Ω_2). Here $k = 2$ terms are used in our error analysis for our simultaneous fit to $\alpha_s(m_Z)$ and Ω_1. The leading power correction that is not fully captured in all regions is of type 3, and are of $\mathcal{O}(\alpha_s\Lambda_{\text{QCD}}/Q)$. Since our analysis is dominated by $Q = m_Z$ or larger, parametrically this gives an uncertainty of

$$\left[\frac{\delta\alpha_s}{\alpha_s}\right]_{\text{p.c.}} \sim \frac{\Lambda_{\text{QCD}}}{Q} \simeq 0.3\% \qquad (10)$$

in our final fit (taking $\Lambda_{\text{QCD}} = 0.3\,\text{GeV}$ to obtain the number here). This estimate has been validated by running our fits in the presence of an additional $\alpha_s\Lambda_{\text{QCD}}/Q$ power correction.[6]

C. Singular Partonic Distribution

The singular partonic thrust distribution $\mathrm{d}\hat\sigma_s/\mathrm{d}\tau$ contains the most singular terms $\propto \alpha_s^j \ln^k(\tau)/\tau$ and $\alpha_s^j\delta(\tau)$ that arise from perturbation theory. Using SCET one can derive a factorization theorem for these terms which allows for the resummation of the logarithmic terms to all orders in perturbation theory. In massless QCD the factorization formula for the perturbative corrections involving α_s reads

$$\frac{\mathrm{d}\hat\sigma_s^{\text{QCD}}}{\mathrm{d}\tau}(\tau) = Q \sum_I \sigma_0^I H_Q^I(Q, \mu_H)\, U_H(Q, \mu_H, \mu)\!\int\! \mathrm{d}s\, \mathrm{d}s'$$

---

[6] To perform this test we include an $\alpha_s(\mu_{\text{ns}})\Lambda_1/Q$ correction in the normalized thrust cross section, vary $\Lambda_1 = \pm1.0\,\text{GeV}$, and perform our default fit to $\alpha_s(m_Z)$ and Ω_1 as described in Sec. VI. This variation causes only a $\pm0.1\%$ change to these fit parameters, which is smaller than the estimate in Eq. (10).

$$\times J_\tau(s', \mu_J)\, U_J^\tau(s - s', \mu, \mu_J) \int \mathrm{d}k'\, U_S^\tau(k', \mu, \mu_S)$$

$$\times e^{-2\frac{\delta(R, \mu_S)}{Q}\frac{\partial}{\partial\tau}}\, S_\tau^{\text{part}}\!\left(Q\tau - \frac{s}{Q} - k', \mu_S\right). \qquad (11)$$

Here σ_0^I is the total partonic e^+e^- cross section for quark pair production at tree level from a current of type $I = \{uv, dv, bv, ua, da, ba\}$ as explained below. Large logs are summed by the renormalization group factors U_H between the hard scale and μ, U_J^τ between the jet scale and μ, and U_S^τ between the soft scale and μ. The choice of μ is arbitrary and the dependence on μ cancels out exactly when working at any particular order in the resummed expansion. Short distance virtual corrections are contained in the hard function H_Q^I. The term J_τ is the thrust jet function. The term S_τ^{part} is the partonic soft function and the $\delta(R, \mu_S)$-dependent exponential implements the perturbative renormalon subtractions. There are four renormalization scales governing the factorization formula, the hard scale $\mu_H \sim Q$, the jet scale μ_J, the soft scale μ_S, and the renormalon subtraction scale R. We have $R \sim \mu_S$ to properly sum logarithms related to the renormalon subtractions, and there is also a renormalization group evolution in R. The typical values for μ_J, μ_S, and R depend on τ as discussed in Sec. III.

The total tree level partonic e^+e^- cross section $\sigma_0^I = \sigma_0^I(Q, m_Z, \Gamma_Z)$ depends on the c.m. energy Q, the Z-mass, and Z-width, and has six types of components, σ_0^{uv}, σ_0^{ua}, σ_0^{dv}, σ_0^{da}, σ_0^{bv}, σ_0^{ba}, where the first index denotes flavor, $u = $ up + charm, $d = $ down + strange, and $b = $ bottom, and the other index denotes production through the vector (v) and axial-vector (a) currents. For QCD corrections we have the hard functions $H_Q^v \equiv H_Q^{uv} = H_Q^{dv} = H_Q^{bv}$, H_Q^{ua}, H_Q^{da}, and H_Q^{ba}, where the vector current terms do not depend on the flavor of the quark. For massless quark production the axial-vector hard functions differ from the vector due to flavor singlet contributions. All six σ_0^I's and H_Q^I's are relevant for

the implementation of the b-mass and QED corrections. Since we use data taken for energies close to the Z pole we adopt $i/(q^2 - m_Z^2 + i\,Q^2\Gamma_z/m_Z)$ as the Z-boson propagator which is the form of the width term used for thrust data analyses. The modifications of Eq. (11) required to include QED effects are discussed in Sec. II H.

The hard factor H_Q contains the hard QCD effects that arise from the matching of the two-jet current in SCET to full QCD. For $\mu_H = Q$ we have $H_Q^v(Q,Q) = 1 + \sum_{j=1}^3 h_j[\alpha_s(Q)/4\pi]^j$, and the full hard function with $\ln(\mu_H/Q)$ dependence is given in Eq. (A6). For the flavor nonsinglet contributions where the final-state quarks are directly produced by the current one can obtain the matching coefficient from the on-shell quark vector current form factor, which is known to $\mathcal{O}(\alpha_s^3)$ [42, 48, 49, 50, 51, 52]. Converting the bare result in Ref. [52] (see also Refs. [42, 53]) to the $\overline{\text{MS}}$ scheme and subtracting $1/\epsilon_{\text{IR}}^k$ divergences present in SCET graphs, the three-loop non-singlet constant, which is one of the new ingredients in our analysis, is

$$
\begin{aligned}
h_3 = &\ C_F^3\bigg[-460\zeta(3) - \frac{140\pi^2\zeta(3)}{3} + 32\zeta(3)^2 + 1328\zeta(5) \\
& - \frac{5599}{6} + \frac{4339\pi^2}{36} - \frac{346\pi^4}{15} + \frac{27403\pi^6}{17010}\bigg] \\
& + C_A C_F^2\bigg[-\frac{52564\zeta(3)}{27} + \frac{1690\pi^2\zeta(3)}{9} + \frac{592\zeta(3)^2}{3} \\
& - \frac{5512\zeta(5)}{9} + \frac{824281}{324} - \frac{406507\pi^2}{972} + \frac{92237\pi^4}{2430} \\
& - \frac{1478\pi^6}{1701}\bigg] + C_A^2 C_F\bigg[\frac{505087\zeta(3)}{243} - \frac{1168\pi^2\zeta(3)}{9} \\
& - \frac{2272\zeta(3)^2}{9} - \frac{868\zeta(5)}{9} - \frac{51082685}{26244} + \frac{596513\pi^2}{2187} \\
& - \frac{4303\pi^4}{4860} + \frac{4784\pi^6}{25515}\bigg] + C_F^2 n_f\bigg[\frac{26080\zeta(3)}{81} - \frac{148\pi^2\zeta(3)}{9} \\
& - \frac{832\zeta(5)}{9} - \frac{56963}{486} + \frac{13705\pi^2}{243} - \frac{1463\pi^4}{243}\bigg] \\
& + C_A C_F n_f\bigg[-\frac{8576\zeta(3)}{27} + \frac{148\pi^2\zeta(3)}{9} - \frac{8\zeta(5)}{3} \\
& + \frac{3400342}{6561} - \frac{201749\pi^2}{2187} - \frac{35\pi^4}{243}\bigg] + C_F n_f^2\bigg[-\frac{832\zeta(3)}{243} \\
& - \frac{190931}{6561} + \frac{1612\pi^2}{243} + \frac{86\pi^4}{1215}\bigg] \\
= &\ 20060.0840 - 2473.4051 n_f + 52.2009 n_f^2 . \quad (12)
\end{aligned}
$$

For $n_f = 5$ we have $h_3 = 8998.080$, which is the value used for our analysis.[7]

The axial-vector hard functions H_Q^{ua} and H_Q^{da} are equal to H_Q^v up to additional singlet corrections that
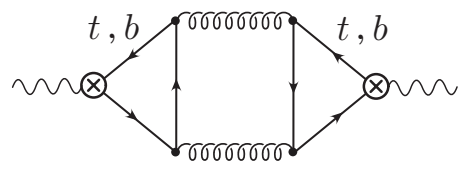

FIG. 2: Two-loop singlet correction to the axial current. Its cuts contribute to the hard coefficient and nonsingular terms.

enter at $\mathcal{O}(\alpha_s^2)$ and $\mathcal{O}(\alpha_s^3)$. The fact that the SCET hard functions have these singlet corrections was discussed in Ref. [55]. At $\mathcal{O}(\alpha_s^2)$ only the axial-vector current gets a singlet correction. It arises from the axial-vector anomaly, from suitable cuts of the graph shown in Fig. 2 where each axial current is connected to a triangle. Summing over the light quarks u, d, s, c gives a vanishing contribution from this graph, but it does not vanish for heavy quarks due to the large bottom-top mass splitting [56]. Since for the Qs we consider top-pairs are never produced, the required terms can be obtained in the limit $m_b/m_t \to 0$. For the axial current the hard correction arises from the $b\bar{b}$ cut and gives $H_Q^{ua} = H_Q^{da} = H_Q^v$, and $H_Q^{ba} = H_Q^v + H_Q^{\text{singlet}}$, where

$$
H_Q^{\text{singlet}}(Q, r_t, \mu_H) = \frac{1}{3}\left(\frac{\alpha_s(\mu_H)}{\pi}\right)^2 I_2(r_t). \quad (13)
$$

Here $r_t = Q^2/(4m_t^2)$ and the function $I_2(r_t)$ from Ref. [56] is given in Eq. (A7). Throughout our analysis we use $m_t = 172\,\text{GeV}$. H_Q^{singlet} is a percent level correction to the cross section at the Z peak and hence is nonnegligible at the level of precision of our analysis. (The uncertainty in the top mass is numerically irrelevant.) At $\mathcal{O}(\alpha_s^3)$ the singlet corrections for vector currents are known [42], but they are numerically tiny. We therefore neglect the $\mathcal{O}(\alpha_s^3)$ vector current singlet corrections together with the unknown $\mathcal{O}(\alpha_s^3)$ singlet corrections for the axial-vector current. Likewise we do not account for $\mathcal{O}(\alpha_s^3)$ singlet corrections to the nonsingular distributions discussed in Sec. II E.

The full anomalous dimension of H_Q^I is known at three-loops, $\mathcal{O}(\alpha_s^3)$ [49, 51, 57]. It contains the cusp anomalous dimension, responsible for the resummation of the Sudakov double logarithms, and the non-cusp anomalous dimension. To determine the corresponding hard renormalization group factor U_H at the orders N³LL′ and N³LL we need the $\mathcal{O}(\alpha_s^4)$ cusp anomalous dimension Γ_3^{cusp} which is still unknown and thus represents a source of theory error in our analysis. We estimate the size of Γ_3^{cusp} from the order $[1/1]$ Padé approximant in α_s built from the known lower order coefficients, which is within 13% of the two other possible Padé approximants, $[0/2]$ and $[0/1]$. For our theory error analysis we assign 200% uncertainty to this estimate and hence scan over values in the range $\Gamma_3^{\text{cusp}} = 1553.06 \pm 3016.12$.

The thrust jet function J_τ is the convolution of the two hemisphere jet functions that describe collinear radiation

---

[7] The analytic expression for h_3 in Eq. (12) is consistent with Eq. (7.3) given in Ref. [54].

in the $\hat{t}$ and $-\hat{t}$ directions,

$$J_\tau(s, \mu) = \int ds' \, J(s', \mu) \, J(s - s', \mu)$$

$$= \frac{1}{\mu^2} \sum_{n=-1}^{\infty} J_n[\alpha_s(\mu)] \mathcal{L}_n(s/\mu^2). \quad (14)$$

Here the coefficients J_n are multiplied by the functions

$$\mathcal{L}_{-1}(x) = \delta(x), \qquad \mathcal{L}_n(x) = \left[\frac{\ln^n x}{x} \right]_+, \quad (15)$$

where $n \geq 0$. Here $\mathcal{L}_{n \geq 0}(x)$ are the standard plus-functions, see Eq. (A17). At $\mathcal{O}(\alpha_s^3)$ only $J_{-1}(\alpha_s)$ through $J_5(\alpha_s)$ are nonzero. The results are summarized in Eq. (A16). In SCET the inclusive jet function is defined as

$$J(Qr^+, \mu) =$$
$$\frac{-1}{4\pi N_c Q} \operatorname{Im}\left[i \int d^4x \, e^{ir \cdot x} \langle 0|\mathrm{T}\{\bar{\chi}_n(0)\hat{\phi}\chi_n(x)\}|0\rangle\right], \quad (16)$$

where the χ_n are quark fields multiplied by collinear Wilson lines. The hemisphere jet function has been computed at $\mathcal{O}(\alpha_s)$ [58, 59] and $\mathcal{O}(\alpha_s^2)$ [60]. Its anomalous dimension is known at three loops, and can be obtained from Ref. [61]. At the order $\mathrm{N}^3\mathrm{LL}'$ we need the $\mathcal{O}(\alpha_s^3)$ corrections to the jet function. From the anomalous dimension we know the logarithmic terms, J_0 to J_{-5} in Eq. (14), at three loops. In the non-logarithmic term J_{-1} at $\mathcal{O}(\alpha_s^3)$ there is an unknown coefficient j_3 (which we define as the constant non-logarithmic 3-loop coefficient in the position space hemisphere jet function). We estimate a range for j_3 from the largest value obtained from the three Padé approximations for the position space hemisphere jet function that one can construct from the available results. This gives $j_3 = 0 \pm 3000$ for the range of variation in our theory error analysis. We note that for the $\mathcal{O}(\alpha_s^3)$ coefficient h_3 the corresponding Padé estimate $h_3 = 0 \pm 10000$ covers the exact value given in Eq. (12).

The renormalization group factors of the thrust jet function U_J^τ and thrust soft function U_S^τ sum up large logs involving the jet and the soft scales. The required cusp and non-cusp anomalous dimensions are fully known at three-loops, but again there is dependence on the four-loop cusp anomalous dimension Γ_3^{cusp}. This dependence is included when we scan this parameter as described above in our description of the hard evolution.

The hadronic thrust soft function S_τ describes soft radiation between the two jets. It is defined by

$$S_\tau(k, \mu) = \frac{1}{N_c} \langle 0|\operatorname{tr} \overline{Y}_{\bar{n}}^T Y_n \, \delta(k - i\hat{\partial}) Y_n^\dagger \overline{Y}_{\bar{n}}^* |0\rangle, \quad (17)$$

where $Y_n = Y_n(0)$ and $\overline{Y}_{\bar{n}} = \overline{Y}_{\bar{n}}(0)$ are defined below Eq. (6). The soft function factorizes into a partonic perturbative part S_τ^{part} and a nonperturbative part S_τ^{mod}, $S_\tau = S_\tau^{\mathrm{part}} \otimes S_\tau^{\mathrm{mod}}$, as discussed in detail in Sec. II D.

This factorization has already been used above in Eqs. (4) and (11).

At the partonic level the soft function is

$$S_\tau^{\mathrm{part}}(k, \mu) = \frac{1}{\mu} \sum_{n=-1}^{\infty} S_n[\alpha_s(\mu)] \mathcal{L}_n(k/\mu), \quad (18)$$

where S_{-1} to S_5 are the only nonzero coefficients at $\mathcal{O}(\alpha_s^3)$, and $\mathcal{L}_n(x)$ is defined in Eq. (15). Results for these $S_k(\alpha_s)$ are summarized in Eq. (A14). S_τ^{pert} was calculated at $\mathcal{O}(\alpha_s)$ in Ref. [14, 15]. At $\mathcal{O}(\alpha_s^2)$ the non-logarithmic correction was determined in Refs. [20, 62] using numerical output from EVENT2 [63, 64]. The numerical constant that appears in the non-logarithmic $\mathcal{O}(\alpha_s^2)$ term S_{-1} is referred to as s_2 (which is defined as the constant 2-loop coefficient in the logarithm of the position space soft function). We use $s_2 = -39.1 \pm 2.5$ [62], and this uncertainty is taken into account in our theory error analysis.[8] The anomalous dimension of the soft function is a linear combination of the anomalous dimensions of the hard and jet functions which can be obtained from the consistency conditions [20, 41]. As for the jet function we need the $\mathcal{O}(\alpha_s^3)$ corrections to S_τ^{part}. From its anomalous dimension we know the logarithmic terms at three loops, namely S_0 to S_5 in Eq. (18). The only unknown is the $\mathcal{O}(\alpha_s^3)$ non-logarithmic correction in S_{-1}, referred to as s_3 (which is defined as the constant non-logarithmic term in the logarithm of the position space hemisphere soft function). Just like for the constant j_3 we estimate a value for s_3 from the largest value obtained from the three possible Padé approximations to the position space soft function that one can construct from the available results. This yields the range $s_3 = 0 \pm 500$, which we scan over in our theory error analysis.

As already mentioned, in Ref. [20] an analytic expression for the resummed singular thrust distribution was presented. Their derivation relies on the Laplace transform of the jet and soft functions. In our analysis we have derived the resummed cross section using two independent procedures, performing all convolutions either in momentum space (as presented in App. A), or in Fourier space. These two approaches have been implemented in two independent codes and we have checked that they give exactly the same results. We note that the Fourier transform method is equivalent to the Laplace procedure used by Becher and Schwartz in Ref. [20] through a contour deformation, and we find agreement with their quoted $\mathrm{N}^3\mathrm{LL}$ formula including matrix elements and anomalous dimensions. Furthermore, we also agree with their result for the fixed-order singular terms up to $\mathcal{O}(\alpha_s^3)$.

In summary, the singular terms in the thrust factorization theorem are known at $\mathrm{N}^3\mathrm{LL}$ order, up to the unknown constant Γ_3^{cusp}. The effect of the cusp anomalous dimension at 4-loops is much smaller than one might

---

[8] Note that in Ref. [62] our s_2 was called s_1.

estimate, so for numerical purposes the cross section is known at this order. The constants s_3 and j_3 only enter for our N^{3}LL$'$ order. For the singular terms they predominantly affect the peak region with spread into the tail region only due to RG evolution. Thus in the tail region the numerically dominant N^{3}LL$'$ terms are all known. The uncertainties from $\Gamma_3^{\rm cusp}$, s_3, and j_3 are discussed more explicitly in Sec. VII

D. Ω_1 and Nonperturbative Corrections

In this section we discuss nonperturbative corrections to the thrust distribution included in our analysis, as shown in Tab. IIb (right panel). We focus in particular on those associated to the first moment parameter Ω_1. Our analysis includes the operator product expansion (OPE) for the soft function in the tail region, and combining perturbative and nonperturbative information to smoothly connect the peak and tail analyses. We also discuss our treatment of nonperturbative corrections in the far-tail region, and for the nonsingular terms in the cross section.

In the tail region where $k \sim Q\tau \gg \Lambda_{\rm QCD}$ we can perform an operator product expansion of the soft function in Eq. (17). At tree level this gives [65, 66]

$$S_\tau(k,\mu) = \delta(k) - \delta'(k)\, 2\bar\Omega_1 + \dots . \qquad (19)$$

where the nonperturbative matrix element $\bar\Omega_1$ is defined in the $\overline{\rm MS}$ scheme as

$$\bar\Omega_1 = \frac{1}{2N_c}\langle 0|{\rm tr}\, \overline{Y}_{\bar n}^T(0)Y_n(0)\, i\widehat\partial\, Y_n^\dagger(0)\overline{Y}_{\bar n}^*(0)|0\rangle . \qquad (20)$$

Dimensional analysis indicates that $\bar\Omega_1 \sim \Lambda_{\rm QCD}$. When the OPE is performed beyond tree level we must add perturbative corrections at a scale $\mu \simeq k$ to Eq. (19). The first operator in the OPE is the identity, and its Wilson coefficient is the partonic soft function. Thus $\delta(k) \rightarrow S_\tau^{\rm part}(k,\mu)$ when the matching of the leading power operator is performed at any fixed order in perturbation theory. Here we derive the analog for the Wilson coefficient of the $\bar\Omega_1$ matrix element and prove that

$$S_\tau(k,\mu) = S_\tau^{\rm part}(k) - \frac{{\rm d}S_\tau^{\rm part}(k)}{{\rm d}k}\, 2\bar\Omega_1 + \dots . \qquad (21)$$

This result implies that the leading perturbative corrections that multiply the power correction are determined by the partonic soft function to all orders in perturbation theory. The proof of Eq. (21) is given in App. B. The uniqueness of the leading power correction $\bar\Omega_1$ to all orders in the perturbative matching can be derived following Ref. [65], and we carry out an all orders matching computation to demonstrate that the Wilson coefficient is ${\rm d}S_\tau^{\rm part}(k)/{\rm d}k$. At first order in $\bar\Omega_1/k \ll 1$ Eq. (21) shows that the perturbative corrections in the OPE are consistent with a simple shift to $S_\tau(k - 2\bar\Omega_1,\mu)$. This

type of shift was first observed in the effective coupling model [35].

To smoothly connect the peak and tail regions we use a factorized soft function [16, 19, 38]

$$S_\tau(k,\mu) = \int{\rm d}k'\, S_\tau^{\rm part}(k-k',\mu)\, S_\tau^{\rm mod}(k') , \qquad (22)$$

where $S_\tau^{\rm part}$ is a fixed-order perturbative $\overline{\rm MS}$ expression for the partonic soft function, and $S_\tau^{\rm mod}$ contains the nonperturbative ingredients. In the tail region this expression can be expanded for $k' \ll k$ and reduces to precisely the OPE in Eq. (21) with the identification

$$2\bar\Omega_1 = \int{\rm d}k'\, k'\, S_\tau^{\rm mod}(k') , \qquad (23)$$

and normalization condition $\int{\rm d}k'\, S_\tau^{\rm mod}(k') = 1$ [16]. All moments of $S_\tau^{\rm mod}(k')$ exist so it has an exponential tail, whereas the tail for $S_\tau^{\rm part}(k)$ is a power law. In the peak region the full nonperturbative function $S_\tau^{\rm mod}(k)$ becomes relevant, and Eq. (22) provides a nonperturbative function whose μ dependence satisfies the $\overline{\rm MS}$ renormalization group equation for the soft function. In position space the convolution in Eq. (22) is a simple product, making it obvious that Eq. (22) provides a completely general parametrization of the nonperturbative corrections. The complete basis of functions used to parameterize $S_\tau^{\rm mod}(k)$ in the peak region is discussed in Sec. IV.

The expression in Eq. (22) also encodes higher order power corrections of type 1 from Eq. (9) through the moments $2^i\bar\Omega_i = \int{\rm d}k\, k^i S_\tau^{\rm mod}(k)$, which for tree level matching in the OPE can be identified as the matrix elements $\langle 0|{\rm tr}\, \overline{Y}_{\bar n}^T(0)Y_n(0)\,(i\widehat\partial)^i Y_n^\dagger(0)\overline{Y}_{\bar n}^*(0)|0\rangle/N_c$. For $i \geq 2$ perturbative α_s corrections to the soft function OPE would have to be treated in a manner similar to App. B to determine the proper Wilson coefficients, and whether additional operators beyond the powers $(i\widehat\partial)^i$ start contributing. The treatment of perturbative corrections to these higher order nonperturbative corrections is beyond the level required for our analysis.

Using Eq. (22) the hadronic version of the singular factorization theorem which involves S_τ immediately yields Eq. (11) and the first term in Eq. (4). The conversion of $S_\tau^{\rm part}(k)$ and $\bar\Omega_1$ from $\overline{\rm MS}$ to a renormalon-free scheme is discussed in Sec. II F.

Next we turn to the effect of $\Lambda_{\rm QCD}$ power corrections on the nonsingular terms in the cross section in Eq. (4). The form of these power corrections can be constrained by factorization theorems for subleading power corrections when $\tau \ll 1$, and by carrying out an OPE analysis for power corrections to the moments of the thrust distribution. In the following we consider both of these.

Based on the similarity of the analysis of power corrections to thrust with those in $B \rightarrow X_s\gamma$ [67, 68], the factorization theorems for the nonsingular corrections involves subleading hard functions, jet functions and soft functions. They have the generic structure $H_Q^{(a,b)}(Q,\tau,x_i)\otimes J_\tau^{(a)}(s_j,x_i)\otimes S_\tau^{(b)}(Q\tau,s_j/Q)$, where the

x_i and s_j are various convolution variables. Here $S_\tau^{(b)}$ includes the leading order soft function in Eq. (17) as well as power suppressed soft functions. Neglecting nonperturbative corrections the nonsingular cross section yields terms we refer to as kinematic power corrections of type 2 in Eq. (9). If we do not wish to sum large logs in the nonsingular partonic terms, they can be treated in fixed-order perturbation theory and determined from the full fixed-order computations. In the tail region these τ-suppressed terms grow and become much more important than the $\Lambda_{\rm QCD}/Q$ power corrections of type 3 from subleading soft functions. In the transition to the far-tail region, near $\tau = 1/3$, they become just as important as the leading perturbative singular terms. In this region there are large cancellations between the singular and nonsingular terms (shown below in Fig. 7), and one must be careful with the treatment of the nonsingular terms not to spoil this.

We require the nonsingular cross section terms to yield perturbative corrections at leading power in $\Lambda_{\rm QCD}$ that are consistent with the fixed-order results and with multijet thresholds. Our treatment of power corrections in the nonsingular terms is done in a manner consistent with these goals and with the OPE for the first moment of the thrust distribution. To achieve this we use

$$\int dk' \frac{d\hat{\sigma}_{\rm ns}}{d\tau}\left(\tau - \frac{k'}{Q}, \frac{\mu_{\rm ns}}{Q}\right) S_\tau^{\rm mod}(k'), \qquad (24)$$

where $d\hat{\sigma}_{\rm ns}/d\tau$ is the partonic nonsingular cross section in fixed-order perturbation theory, whose determination we discuss in Sec. II E. Eq. (24) is independent of the renormalization scale $\mu_{\rm ns}$ order by order in its series expansion in $\alpha_s(\mu_{\rm ns})$. The convolution with the same $S_\tau^{\rm mod}(k')$ as the singular terms allows the perturbative corrections in $d\hat{\sigma}_s/d\tau + d\hat{\sigma}_{\rm ns}/d\tau$ to smoothly recombine into the fixed-order result in the far-tail region as required by the multijet thresholds. Eq. (24) yields the second term in Eq. (4). We will treat the conversion of $\bar{\Omega}_1$ and $S_\tau^{\rm mod}$ to a renormalon-free scheme in the same manner as for the singular cross section, which again for consistency requires a perturbative subtraction for the partonic $d\hat{\sigma}_{\rm ns}/d\tau$ that we treat in Sec. II F.

Note that Eq. (24) neglects the fact that not all of the τ dependence in $d\hat{\sigma}_{\rm ns}/d\tau$ must necessarily be convoluted with $S_\tau^{\rm mod}$. This causes a deviation which is $\sim \alpha_s \tau \Lambda_{\rm QCD}/(Q\tau)$ and hence is at the same level as other power corrections that we neglect. The largest uncertainty from our treatment of $d\hat{\sigma}_{\rm ns}/d\tau$ arises from the fact that we do not sum $\ln \tau$ terms, which would require anomalous dimensions for the subleading soft and hard functions for these nonsingular terms. These logs are most important in the peak region, and less relevant in the tail region. The size of missing higher order nonsingular terms such as log enhanced terms will be estimated by varying the scale $\mu_{\rm ns}$.

Our setup is also consistent with the OPE for the first moment of the thrust distribution. Eq. (4) yields

$$\int d\tau\, \tau \frac{d\sigma}{d\tau} = \int d\tau\, \tau \left[\frac{d\hat{\sigma}_s}{d\hat{\tau}} + \frac{d\hat{\sigma}_{\rm ns}}{d\hat{\tau}}\right] + \sum_I \sigma_0^I \frac{2\bar{\Omega}_1}{Q} + \dots, \qquad (25)$$

where the ellipses denote $\mathcal{O}(\alpha_s \Lambda_{\rm QCD}/Q)$ and $\mathcal{O}(\Lambda_{\rm QCD}^2/Q^2)$ power corrections. In App. C we demonstrate that a direct OPE computation for the thrust moment also gives the same result, and in particular involves precisely the same matrix element $\bar{\Omega}_1$ at this order. The theoretical expression in Eq. (4) simultaneously includes the proper matrix elements that encode power corrections in the peak region, tail region, and for moments of the thrust distribution. This implies a similar level of precision for the multijet region. Although Eq. (4) does not encode all $\alpha_s \Lambda_{\rm QCD}/Q$ corrections, it turns out that the ones it does encode, involving Ω_1, numerically give an accurate description of the multijet cross section. (This is visible in Fig. 18 and will be discussed further in Sec. VII.) This agreement provides additional support for our treatment of nonperturbative corrections in the nonsingular cross section in Eq. (24).

E. Nonsingular Distribution

The nonsingular partonic thrust distribution $d\hat{\sigma}_{\rm ns}/d\tau$ accounts for contributions in the thrust distribution that are kinematically power suppressed. We write

$$\frac{d\hat{\sigma}_{\rm ns}}{d\tau}(\tau) = \sum_I \sigma_0^I\, e^{-2\frac{\delta(R,\mu_s)}{Q}\frac{\partial}{\partial\tau}} f^I\left(\tau, \frac{\mu_{\rm ns}}{Q}\right), \qquad (26)$$

with the same superscript I notation for different currents as in Eq. (11). The presence of the $\delta(R, \mu_S)$-dependent exponent arises because $S_\tau^{\rm mod}$ depends on Ω_1 and we use the same renormalon-free definition for Ω_1 as for the singular terms. In our numerical evaluation we integrate by parts so that the $\partial/\partial\tau$ derivative acts on $S_\tau^{\rm mod}$ in Eq. (4). This exponent is discussed in detail in Sec. II F.

In this section we discuss our determination of the functions f^I in pure QCD with massless quarks, while the generalization to include m_b effects is discussed in Sec. II G and to include QED effects in Sec. II H. For pure QCD there is one function $f_{\rm qcd}^v = f_{\rm qcd}^{uv} = f_{\rm qcd}^{dv} = f_{\rm qcd}^{bv}$ for the vector current, and functions $f_{\rm qcd}^{ua} = f_{\rm qcd}^{da}$, and $f_{\rm qcd}^{ba}$ for the axial-vector currents. In general f^I is the partonic fixed-order distribution where the singular terms which are already contained in $d\hat{\sigma}_s/d\tau$ are subtracted to avoid double counting. Setting the renormalization scale $\mu_{\rm ns} = Q$ they have the form

$$f_{\rm qcd}^v(\tau, 1) = \frac{\alpha_s}{2\pi} f_1(\tau) + \frac{\alpha_s^2}{(2\pi)^2} f_2(\tau) + \frac{\alpha_s^3}{(2\pi)^3} f_3(\tau) + \dots,$$

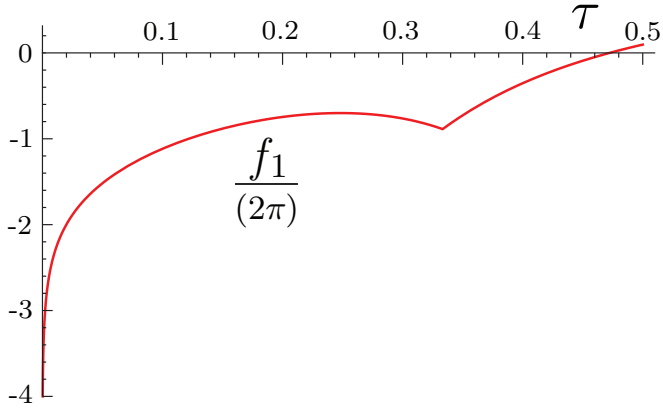$$f_{\rm qcd}^{ua}(\tau, 1) = f_{\rm qcd}^{da}(\tau, 1) = f_{\rm qcd}^v(\tau, 1),$$

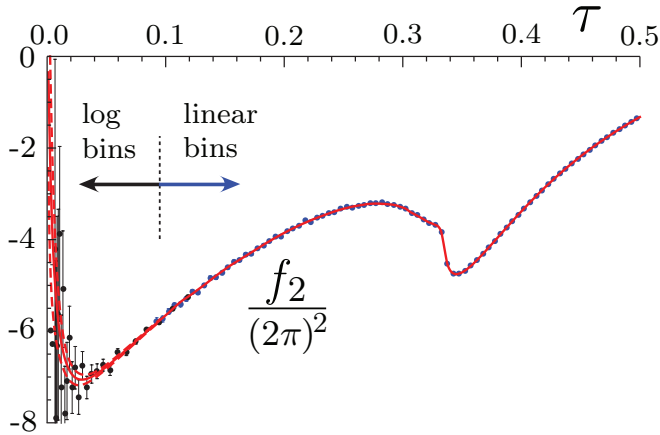FIG. 3: $\mathcal{O}(\alpha_s)$ nonsingular thrust distribution.

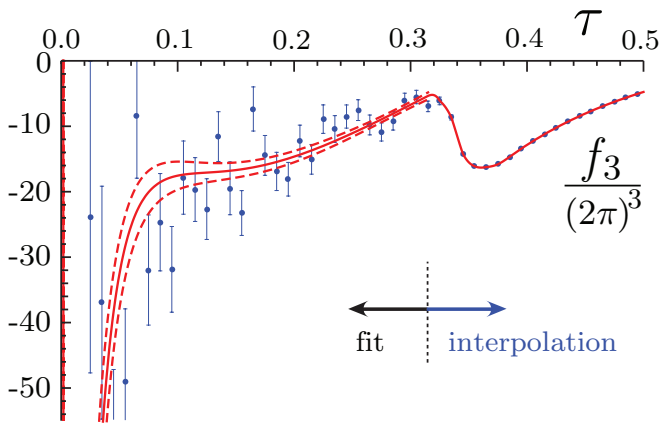FIG. 4: $\mathcal{O}(\alpha_s^2)$ nonsingular thrust distribution.

FIG. 5: $\mathcal{O}(\alpha_s^3)$ nonsingular thrust distribution. For simplicity we only show the data binned with 0.01 bin size.

$$f_{\mathrm{qcd}}^{ba}(\tau, 1) = f_{\mathrm{qcd}}^{v}(\tau, 1) + \frac{\alpha_s^2}{(2\pi)^2} f_{\mathrm{singlet}}\left(\tau, r_t\right), \qquad (27)$$

where here $\alpha_s = \alpha_s(Q)$ and $r_t = Q^2/(4m_t^2)$. The required results for $f^I(\tau, \mu_{\mathrm{ns}}/Q)$ can be obtained by shifting $\alpha_s(Q)$ to $\alpha_s(\mu_{\mathrm{ns}})$ using the fixed-order relation between these couplings at $\mathcal{O}(\alpha_s^2)$.

The full $\mathcal{O}(\alpha_s)$ partonic thrust distribution has been known analytically for a long time [69]. For the one-loop nonsingular distribution it gives

$$f_1(\tau) = \frac{4}{3\,\tau\,(\tau - 1)}\left[\left(-6\,\tau^2 + 6\,\tau - 4\right)\log\left(\frac{1}{\tau} - 2\right)\right.$$
$$\left. + 9\,\tau^3 - 3\,\tau^2 - 9\,\tau + 3\right]\theta\left(\frac{1}{3} - \tau\right) + \frac{4}{3\,\tau}\left[3 + 4\log(\tau)\right].$$
$$(28)$$

This result is plotted in Fig. 3. The kink at $\tau = 1/3$ appears because the full one-loop distribution vanishes at this value with a nonzero slope, and there is an exact cancellation between the fixed-order singular and non-singular one-loop expressions. For $\tau > 1/3$ the one-loop nonsingular distribution is precisely the negative of the one-loop fixed-order singular distribution.

The $\mathcal{O}(\alpha_s^2)$ and $\mathcal{O}(\alpha_s^3)$ QCD distributions are available in numeric form from the Fortran programs EVENT2 [63, 64] and EERAD3 [3] (see also Ref. [4, 5, 6]), respectively. These programs are used to derive results for our $f_2(\tau)$ and $f_3(\tau)$ nonsingular distributions in a manner discussed below. At $\mathcal{O}(\alpha_s^2)$ there is also the singlet correction $f_{\mathrm{singlet}}(\tau, r)$ for the axial-vector contribution arising from the large bottom-top mass splitting. The three-parton quark-antiquark-gluon cut from Fig. 2 contributes to the nonsingular distribution, and we have included this contribution analytically [70]. The formula for $f_{\mathrm{singlet}}(\tau, r)$ is given in Eq. (A30). There is also a contribution from the four-parton cut. Its contribution to $f_{\mathrm{singlet}}(\tau, r)$ is unknown, but it is tiny for the total cross section [56] and can therefore be safely neglected.

At $\mathcal{O}(\alpha_s^2)$ we use linear binned EVENT2 results for $\tau > 0.095$ and log-binning results for $\tau < 0.095$ each obtained from runs with 10^{10} events and infrared cut-off $y_0 = 10^{-8}$. For $\tau > 0.095$ (using a 0.005 bin size) the resulting statistical uncertainties in the nonsingular distribution are always below the percent level and negligible and we can use an interpolation of numerical tables for $f_2(\tau)$. For $\tau < 0.095$ the singular terms dominate the distribution which leads to large cancellations and an enhancement of the statistical uncertainties. Here we use the ansatz $f_2(\tau) = \sum_{i=0}^{3} a_i \ln^i \tau + \tau \sum_{i=2}^{3} b_i \ln^i \tau$ and fit the coefficients a_i and b_i to the EVENT2 output, including the constraint that the integral over the full distribution reproduces the known $\mathcal{O}(\alpha_s^2)$ coefficient for the total cross section. The result has the form $f_2(\tau) + \epsilon_2\,\delta_2(\tau)$, where f_2 represents the best fit and δ_2 is the 1-sigma error function with all correlations included. The term ϵ_2 is a parameter which we vary during our α_s-Ω_1 fit procedure to account for the error. Here f_2 and δ_2 also depend on the coefficient s_2 in the partonic soft function S_τ which is known only numerically. In Fig. 4 we plot the EVENT2 data we used, along with our $f_2(\tau)$ with $s_2 = -39.1$. The dashed curves show the result for $\epsilon_2 = \pm 1$, with the region inbetween corresponding to the 1-sigma error band.

For the determination of f_3 at $\mathcal{O}(\alpha_s^3)$ we implement a similar approach as for f_2, using results from EERAD3 [3]

computed with 6×10^7 events for the three leading color structures and 10^7 events for the three subleading ones, using an infrared cutoff $y_0 = 10^{-5}$. We employ linearly binned results with 0.01 bin size for $\tau > 0.315$ (keeping the statistical error below the percent level) and with 0.005 bin size for $\tau < 0.315$. For the fit for $\tau < 0.315$ our ansatz function has the form $f_3(\tau) = \sum_{i=1}^{5} c_i \ln^i \tau$ and the result has the form $f_3(\tau) + \epsilon_3 \delta_3(\tau)$, with f_3 being the best fit and δ_3 the 1-sigma error function. The constant ϵ_3 is the analog of ϵ_2 and is varied in the error analysis. We note that f_3 and δ_3 depend on the constant s_2 and on the constants s_3 and j_3 that account for the unknown non-logarithmic terms in the $\mathcal{O}(\alpha_s^3)$ soft and jet functions. This dependence is included in our error analysis. In Fig. 5 we plot the EERAD3 data with bin size 0.01, along with our $f_3(\tau)$ with $s_2 = -39.1$, $h_3 = 8998.08$, $j_3 = s_3 = 0$. The dashed curves show the result for $\epsilon_3 = \pm 1$, with the region inbetween corresponding to the 1-sigma error band.

In our analysis we use the values $-1, 0, 1$ for ϵ_2 and ϵ_3 to account for the numerical uncertainties of our fit functions in the small τ region. The nonsingular partonic distribution depends on one common renormalization scale μ_{ns} which is varied in our theory error analysis as given in Sec. III.

F. Gap Formalism

The partonic soft function $S_\tau^{\mathrm{part}}(k)$ computed perturbatively in $\overline{\mathrm{MS}}$ has an $\mathcal{O}(\Lambda_{\mathrm{QCD}})$ renormalon ambiguity. The same renormalon is present in the partonic $\overline{\mathrm{MS}}$ thrust cross section with or without resummation. This is associated with the fact that the partonic threshold at $k = 0$ in $S_\tau^{\mathrm{part}}(k)$ is not the same as the physical hadronic threshold for the distribution of soft radiation that occurs in $S_\tau(k)$. One can see this explicitly in the large-β_0 approximation, where it is associated to a pole at $u = 1/2$ in the Borel transform [16]

$$B\left[S_\tau^{\mathrm{part}}(k,\mu)\right]\left(u \approx \frac{1}{2}\right) = \mu \frac{16 C_F e^{-5/6}}{\pi \beta_0 \left(u - \frac{1}{2}\right)} \frac{\partial}{\partial k} S_\tau^{\mathrm{part}}(k,\mu).$$
(29)

This result shows that $S_\tau^{\mathrm{part}}(k)$ in the $\overline{\mathrm{MS}}$ scheme suffers from the renormalon ambiguity for all $k \geq 0$. The $\overline{\mathrm{MS}}$ matrix element $\bar{\Omega}_1$ defined in Eq. (20) also has an $\mathcal{O}(\Lambda_{\mathrm{QCD}})$ renormalon ambiguity. Together, the renormalon in this power correction and in the perturbative series for $S_\tau^{\mathrm{part}}(k)$ combine to give a soft function $S_\tau(k)$ that is free from this $\mathcal{O}(\Lambda_{\mathrm{QCD}})$ renormalon. If left unsubtracted this renormalon ambiguity leads to numerical instabilities in perturbative results for the thrust distribution and in the large order dependence for the determination of the soft nonperturbative function S_τ^{mod}. In this section we resolve this problem by switching to a new scheme for Ω_1. This scheme change induces subtractions

on $d\sigma^{\mathrm{part}}/d\tau$ that render it free of this renormalon. We start by reviewing results from Ref. [16].

Consider a class of soft nonperturbative functions with a gap parameter Δ, which only have support for $k \geq \Delta$, so $S_\tau^{\mathrm{mod}}(k) \to S_\tau^{\mathrm{mod}}(k - 2\Delta)$. Here the $\overline{\mathrm{MS}}$ moment relation in Eq. (23) becomes

$$2\Delta + \int dk \, k \, S_\tau^{\mathrm{mod}}(k) = 2\bar{\Omega}_1 ,$$
(30)

where Δ accounts for the complete renormalon ambiguity contained in $\bar{\Omega}_1$. We can now obtain a renormalon-free definition for Ω_1 by splitting Δ into a nonperturbative component $\bar{\Delta}(R, \mu_S)$ that is free of the $\mathcal{O}(\Lambda_{\mathrm{QCD}})$ renormalon, and a suitably defined perturbative series $\delta(R, \mu_S)$ that has the same renormalon ambiguity as $\bar{\Omega}_1$. The parameter Δ is scheme and renormalization group invariant, while $\bar{\Delta}$ and δ individually depend on the subtraction scale R and in general also on the soft scale μ_S. Writing

$$\Delta = \bar{\Delta}(R, \mu_S) + \delta(R, \mu_S) ,$$
(31)

the factorization of perturbative and nonperturbative components in Eq. (22) becomes

$$S_\tau(k, \mu_S) = \int dk' \, S_\tau^{\mathrm{part}}(k - k' - 2\delta, \mu_S) \, S_\tau^{\mathrm{mod}}(k' - 2\bar{\Delta})$$
$$= \int dk' \left[e^{-2\delta \frac{\partial}{\partial k}} S_\tau^{\mathrm{part}}(k - k', \mu_S) \right] S_\tau^{\mathrm{mod}}(k' - 2\bar{\Delta}).$$
(32)

Here the exponential operator induces perturbative subtractions (in powers of $\alpha_s(\mu_S)$) on the $\overline{\mathrm{MS}}$ series in $S_\tau^{\mathrm{part}}(k)$ that render it free of the renormalon. This exponential modifies perturbative results for the cross section in the manner we have shown earlier in Eqs. (11) and (26). The convolution of the nonsingular cross-section with S_τ^{mod} in Eq. (24) now becomes

$$\int dk' \frac{d\hat{\sigma}_{\mathrm{ns}}}{d\tau}\left(\tau - \frac{k'}{Q}, \frac{\mu_{\mathrm{ns}}}{Q}\right) S_\tau^{\mathrm{mod}}(k' - 2\bar{\Delta}).$$
(33)

Furthermore, with Eq. (32) the result in Eq. (30) becomes

$$2\bar{\Delta}(R, \mu_S) + \int dk \, k \, S_\tau^{\mathrm{mod}}(k) = 2\Omega_1(R, \mu_S) ,$$
(34)

where here $\Omega_1(R, \mu_S)$ is renormalon-free. Combining Eqs. (34) and (30) we see that the scheme conversion formula from $\overline{\mathrm{MS}}$ to the new scheme is

$$\Omega_1(R, \mu_S) = \bar{\Omega}_1 - \delta(R, \mu_S).$$
(35)

Thus, the precise scheme for $\Omega_1(R, \mu_S)$ is specified by the choice of the subtraction series $\delta(R, \mu_S)$. Note that in general the gap parameter $\bar{\Delta}$ is an additional nonperturbative parameter that can be determined together with other parameters in the function S_τ^{mod} from fits to experimental data. However, in the tail region the power corrections are dominated by a single parameter, $\Omega_1(R, \mu_S)$, which encodes the dependence on $\bar{\Delta}$.

In Ref. [62] a convenient scheme for $\delta(R,\mu_S)$ was derived (based on a scheme proposed in Ref. [71]) where

$$\delta(R,\mu) = \frac{R}{2}\, e^{\gamma_E}\, \frac{d}{d\ln(ix)}\Big[\ln S_\tau(x,\mu)\Big]\Big|_{x=(iRe^{\gamma_E})^{-1}}. \quad (36)$$

Here $S_\tau(x,\mu)$ is the position space partonic soft function, and the fact that we write this result for S_τ rather than for the hemisphere soft function explains the extra factor of $1/2$ relative to the formula in Ref. [62]. The cutoff parameter R, having mass dimension 1, is a scale associated with the removal of the infrared renormalon. To achieve the proper cancellation of the renormalon in Eq. (32) one has to expand $\delta(R,\mu_S)$ together with $S_\tau^{\mathrm{part}}(k,\mu_S)$ order by order in $\alpha_s(\mu_S)$. The perturbative series for the subtraction is

$$\delta(R,\mu_S) = e^{\gamma_E} R \sum_{i=1}^{\infty} \alpha_s^i(\mu_S)\, \delta_i(R,\mu_S)\,, \quad (37)$$

where the $\delta_{i\geq2}$ depend on both the adjoint Casmir $C_A = 3$ and the number of light flavors in combinations that are unrelated to the QCD beta function. For five light flavors the one, two, and three-loop coefficients are [62]

$$\delta_1(R,\mu_S) = -0.848826 L_R\,,$$
$$\delta_2(R,\mu_S) = -0.156279 - 0.46663 L_R - 0.517864 L_R^2\,,$$
$$\delta_3(R,\mu_S) = 0.0756831 + 0.01545386\, s_2 - 0.622467 L_R$$
$$\qquad - 0.777219 L_R^2 - 0.421261 L_R^3\,, \quad (38)$$

with $L_R = \ln(\mu_S/R)$. We will refer to the scheme defined by Eq. (36) as the R-gap scheme for Ω_1.

From the power counting $\bar\Omega_1 \sim \Lambda_{\mathrm{QCD}}$ one expects that a cutoff $R \sim 1$ GeV should be used, such that $\Omega_1 \sim \Lambda_{\mathrm{QCD}}$ and perturbation theory in $\alpha_s(R)$ remains applicable. We refer to this as the power counting criterion for R. Since in the tail region $\mu_S \sim Q\tau \gg 1$ GeV the factors of L_R in Eq. (38) are then large logs. To avoid large logarithms in the subtractions $\delta_i(R,\mu_S)$ it is essential to choose $R \sim \mu_S$, so that the subtraction scale R is dependent on τ much like the soft scale μ_S. We refer to this as the large-log criterion for R. To resolve the conflict between these two criteria, and sum the large logs while keeping $\bar\Delta(R,\mu_S \sim R)$ renormalon-free, we make use of R-evolution [39, 40]. Formulas for the gap case were given in Ref. [62] and are reviewed here. In this scheme $\bar\Delta(R,\mu)$ satisfies an R-RGE and μ-RGE

$$R\frac{d}{dR}\bar\Delta(R,R) = -R\sum_{n=0}^{\infty} \gamma_n^R \left(\frac{\alpha_s(R)}{4\pi}\right)^{n+1}\,,$$
$$\mu\frac{d}{d\mu}\bar\Delta(R,\mu) = 2Re^{\gamma_E}\sum_{n=0}^{\infty} \Gamma_n^{\mathrm{cusp}}\left(\frac{\alpha_s(\mu)}{4\pi}\right)^{n+1}\,, \quad (39)$$

so that $\gamma_\Delta^\mu = -2e^{\gamma_E}\Gamma^{\mathrm{cusp}}[\alpha_s]$. For five flavors the anomalous dimension coefficients up to three loops are

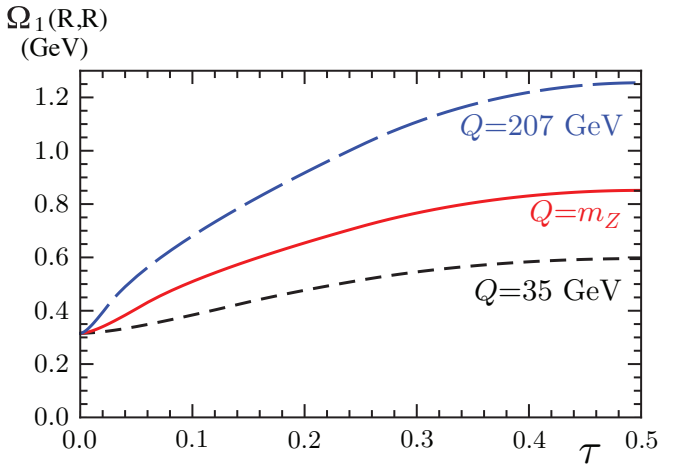$$\gamma_0^R = 0\,, \qquad \gamma_1^R = -43.954260\,,$$

FIG. 6: The running of $\Omega_1(R,R)$ with $R = R(\tau)$, plotted as a function of τ for $Q = 35, 91.2, 207$ GeV.

$$\gamma_2^R = 1615.42228 + 54.6195541\, s_2\,, \quad (40)$$

while the coefficients Γ_n^{cusp} are given in Eq. (A26). The solution of Eq. (39) at $\mathrm{N}^k\mathrm{LL}$ is

$$\bar\Delta(R,\mu) = \bar\Delta(R_\Delta,\mu_\Delta) + Re^{\gamma_E}\omega[\Gamma^{\mathrm{cusp}},\mu,R]$$
$$\qquad + R_\Delta e^{\gamma_E}\omega[\Gamma^{\mathrm{cusp}},R_\Delta,\mu_\Delta]$$
$$\qquad + \Lambda_{\mathrm{QCD}}^{(k)} D^{(k)}\big[\alpha_s(R),\alpha_s(R_\Delta)\big]\,, \quad (41)$$

where the resummed $\omega[\Gamma^{\mathrm{cusp}},\mu,\mu_0]$ is given in Eq. (A23) and the resummed $D^{(k)}[\alpha_s(R),\alpha_s(R_\Delta)]$ is given in Eq. (A31). Both the gap subtraction and R-evolution equations at $\mathcal{O}(\alpha_s^3)$ depend on the constant s_2 which we vary within its errors in our theory error scan. In our analysis, when quoting numerical results, we always use the parameter $\bar\Delta(R_\Delta,\mu_\Delta)$ at the reference scales $R_\Delta = \mu_\Delta = 2$ GeV to satisfy the power counting criterion for R. We then use Eq. (41) to run up to the scale $R \sim \mu_S$ in order to satisfy the large-log criterion. The precise R value is a function of τ, $R = R(\tau)$, and given in Sec. III with our discussion of the profile functions. The RGE solution for $\bar\Delta(R,\mu_S)$ in Eq. (41) yields a similar solution for a running $\Omega_1(R,\mu_S)$ using Eq. (34). In Fig. 6 we show the result for the running $\Omega_1(R,R)$ with the boundary value $\Omega_1(R_\Delta,\mu_\Delta) = 0.323$ GeV. The anomalous dimension and $R(\tau)$ profile function cause an increase in the size of the power correction for increasing τ and for increasing Q.

Note that our R-gap subtraction scheme differs from the subtractions in the low-scale effective coupling model of Ref. [35], which is not based on the factorization of the soft large angle radiation but on the assumption that the $\mathcal{O}(\Lambda_{\mathrm{QCD}})$ renormalon ambiguity is related entirely to the low-energy behavior of the strong coupling α_s. In the effective coupling model the subtractions involve logarithms, $\ln(\mu/\mu_I)$, where μ is the usual renormalization scale of perturbation theory and μ_I is the low-momentum subtraction scale, which is set to $\mu_I = 2$ GeV. The scale
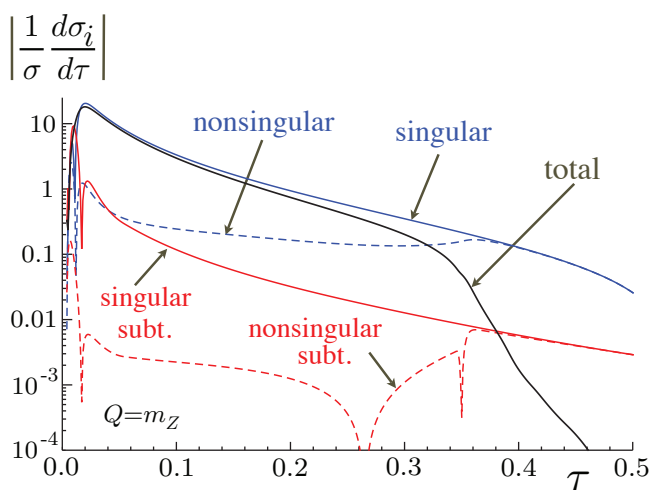
FIG. 7: Components of the pure QCD cross section. Here $\Omega_1 = 0.35$ GeV and $\alpha_s(m_Z) = 0.114$.

μ_I plays a role very similar to the scale R in the R-gap scheme. These logarithms are the analogs of L_R in Eq. (38) and, since $\mu \propto Q$ these logarithms also become large. In the effective coupling model an appropriate resummation formalism for large logs in the subtractions remains an open question.

In Fig. 7 we plot the absolute value of four components of our cross section for our complete QCD result at N³LL′ order in the R-gap scheme at $Q = m_Z$. The cross section components include the singular terms (solid blue), nonsingular terms (dashed blue), and separately the contributions from terms that involve the subtraction coefficients δ_i, for both singular subtractions (solid red) and nonsingular subtractions (dashed red). The sum of these four components gives the total cross section (solid black line). The subtraction components are a small part of the cross section in the tail region, but have an impact at the level of precision obtained in our computation. In the peak region at very small τ the solid red singular subtraction grows to be the same size as the solid blue singular term, and is responsible for yielding a smooth positive definite total cross section. In both the peak and tail regions the singular cross section dominates over the nonsingular cross section. But as we approach the threshold $\tau \sim 1/3$ for the far-tail region they appear with opposite signs and largely cancel. This is clear from the figure where individually the singular and nonsingular lines are larger than the total cross section in this region. The same cancellation occurs for the singular subtraction and nonsingular subtraction terms.

G. Bottom Mass Effects

In this work we implement bottom mass effects using the SCET factorization framework for massive quarks [14, 41]. We include m_b-dependence in the kine-

matics, which starts at tree level, and in the $\mathcal{O}(\alpha_s)$ corrections in the partonic singular and nonsingular distributions. We also account for the resummation of large logs and for hadronization effects in the m_b-dependent terms. The mass dependent factorization theorem implies that the renormalization group summation of logarithms is identical to the one for massless quarks, and that all power corrections of type 1 from Eq. (9) are described by the nonperturbative soft function S_τ^{mod} already defined for the massless case [14, 41]. We have already indicated this with the convolution $\Delta d\hat{\sigma}_b/d\tau \otimes S_\tau^{\mathrm{mod}}$ shown in Eq. (4). Since for the numerical analysis in this work we fit to data in the tail region, where $Q\tau > 6$ GeV, and since the massive quark thrust factorization theorem implies for the soft scale $\mu_S \sim Q\tau > 6$ GeV, we do not have to account for any flavor threshold in the renormalization group evolution and can always use $n_f = 5$. The mass dependent factorization theorem further implies that the only nontrivial m_b-dependence in the singular distribution arises in the thrust jet function. Thus the jet scale $\mu_J \sim Q\sqrt{\tau} \gg m_b$ for the region of our fit and we use the $\overline{\mathrm{MS}}$ bottom mass $\overline{m}_b(\mu_J)$ to parameterize the m_b corrections with $\bar{m}_b(\bar{m}_b) = 4.2$ GeV as our input value. Using the $\overline{\mathrm{MS}}$ mass rather than the pole mass avoids the appearance of large higher order effects related to the $\mathcal{O}(\Lambda_{\mathrm{QCD}})$ pole mass renormalon.

We implement the partonic bottom mass corrections as an additive term to the massless partonic N³LL′ cross section. These corrections come from the production of bottom quarks by the virtual γ or Z,

$$\frac{\Delta d\hat{\sigma}_b}{d\tau} = \frac{d\hat{\sigma}_b}{d\tau} - \frac{d\hat{\sigma}_b^{\bar{m}_b=0}}{d\tau}, \tag{42}$$

where both $d\hat{\sigma}_b/d\tau$ and $d\hat{\sigma}_b^{\bar{m}_b=0}/d\tau$ are computed at NNLL. Because the effect of $\bar{m}_b \neq 0$ in $\Delta d\hat{\sigma}_b/d\tau$ is expected to be a percent level correction to the tail cross section, we anticipate that the NNLL level of precision suffices. (This is also justified a posteriori by the relatively small effect of the m_b corrections on our fit results.)

An important aspect in the discussion of the finite quark mass effects is in which way hadron and heavy quark masses need to be accounted for in the definition of thrust in Eq. (1). In the experimental analyses Monte Carlo generators are used to convert the actual measurements to the momentum variables needed to compute τ, and this conversion depends on hadron masses. Since the final state stable hadrons are light, these effects are related to nonperturbative physics. Theoretically they are therefore implicitly encoded within our fit of the nonperturbative corrections. In the partonic theoretical computation light hadron masses are neglected in the computation of the τ distribution, and it is consistent to set $\sum_i |\vec{p}_i| = Q$ in the denominator of Eq. (1).

To understand how the heavy quark masses affect the definition of thrust in Eq. (1) we recall that the partonic computation relies on the inclusive nature of the measurements and that, experimentally, only light and long-lived hadrons reach the detectors and are accounted for

in the $\vec{p}_i$ momenta that enter in computing τ. Thus for heavy hadrons containing bottom (or charm) quarks, it is their light and long-lived hadronic decay products that enter the particle sum $\sum_i$. Due to energy conservation it is therefore necessary to set $\sum_i |\vec{p}_i| = Q$ in the denominator of the thrust definition of Eq. (1) for the leading power partonic computations involving heavy quarks. On the other hand, due to three-momentum conservation, it is consistent to use the heavy quark three-momentum in the numerator of Eq. (1) for the partonic computations. This makes the partonic thrust computations involving heavy quarks simple because we do not need to explicitly account for the heavy quark decay in the calculations. Together with the relation $\sum_i |\vec{p}_i| = Q$ in the denominator of Eq. (1) this induces a shift of the observed thrust distribution for b quarks to larger τ values. Comparing to the massless quark situation, the small-τ endpoint is moved from 0 to

$$\tau_b^{\min} = 1 - \sqrt{1 - 4\bar{m}_b^2/Q^2}\,, \qquad (43)$$

where here $\bar{m}_b = \bar{m}_b(\mu_J)$. At tree level this shifts $\delta(\tau) \rightarrow \delta(\tau - \tau_b^{\min})$. For the fixed-order result at $\mathcal{O}(\alpha_s)$ the three-jet endpoint is moved from $1/3$ to $\tau_b^{3\text{jet}} = 5/3 - 4/3\sqrt{1 - 3\bar{m}_b^2/Q^2}$. At leading order in $\bar{m}_b^2/Q^2 \ll 1$ we have $\tau_b^{\min} = 2\bar{m}_b^2/Q^2 + \mathcal{O}(\bar{m}_b^4/Q^4)$ and $\tau_b^{3\text{jet}} = 1/3 + 2\bar{m}_b^2/Q^2 + \mathcal{O}(\bar{m}_b^4/Q^4)$, so the shift is the same for both endpoints. Numerically, for $\bar{m}_b = 4.2\,\text{GeV}$ and $Q = (35, 91.2, 207)\,\text{GeV}$, τ is shifted by $(0.029, 0.004, 0.0008)$. This shift is also observed experimentally in flavor tagged thrust analyses [72, 73, 74].

In the following we outline the method used to compute the partonic $d\hat{\sigma}_b/d\tau$. Like for the massless case the distribution is divided into singular and nonsingular parts

$$\frac{d\hat{\sigma}_b}{d\tau} = \frac{d\hat{\sigma}_b^{\text{s}}}{d\tau} + \frac{d\hat{\sigma}_b^{\text{ns}}}{d\tau}\,. \qquad (44)$$

The implementation of the bottom mass effects into the singular distribution $d\hat{\sigma}_b^{\text{s}}/d\tau$ follows the NLL$'$ analysis in Ref. [41], except that the evolution in the present work is incorporated fully at NNLL order and that the exact partonic threshold at $\tau = \tau_b^{\min}$ is accounted for,

$$\frac{d\hat{\sigma}_b^{\text{s}}}{d\tau} = Q\,\sigma_0^b\Big(\frac{\bar{m}_b}{Q}\Big)\,H_Q^v(Q, \mu_H)\,U_H(Q, \mu_H, \mu)\!\int\! ds\,ds'$$

$$\times\,J_{\tau b}(s', \bar{m}_b, \mu_J)\,U_J^\tau(s - s', \mu, \mu_J)\int\! dk\,U_S^\tau(k, \mu, \mu_S)$$

$$\times\,e^{-2\frac{\delta(R,\mu_s)}{Q}\frac{\partial}{\partial\tau}}\,S_\tau^{\text{part}}\Big(Q\tau - Q\tau_b^{\min} - \frac{s}{Q} - k, \mu_S\Big)$$

$$+\,(\overline{\text{MS}}\text{-pole mass scheme change terms})\,, \qquad (45)$$

where $\sigma_0^b(x) = \sigma_0^{bv}\sqrt{1 - 4x^2}(1 + 2x^2) + \sigma_0^{ba}(1 - 4x^2)^{3/2}$. Perturbative bottom mass effects in the soft function start at two loops, so at $\mathcal{O}(\alpha_s)$ S_τ^{part} remains unchanged. Since we have $\bar{m}_b/Q \ll 1$, only the thrust jet function for bottom quark production, $J_{\tau b}(s, \bar{m}_b, \mu)$ [75], receives

modifications from the finite m_b. These modifications lead to a shift of the partonic threshold of the thrust jet function from invariant mass $p^2 = 0$ to $p^2 = \bar{m}_b^2$. In $J_{\tau b}(s, \bar{m}_b, \mu)$ the variable $s = p^2 - \bar{m}_b^2$, and the presence of the mass leads to $\tau_b^{\min}$ in Eq. (45). It also gives a more complicated form for $\mathcal{O}(\alpha_s)$ corrections in $J_{\tau b}$ involving regular functions of m_b^2/s in addition to singular terms $\propto \delta(s)$ and $[\ln^k(s/\mu^2)/(s/\mu^2)]_+$ familiar from the massless quark jet function. More details and explicit formulae can be found in Refs. [14, 41].

The bottom quark mass effects in the nonsingular partonic distribution $d\hat{\sigma}_b^{\text{ns}}/d\tau$ are more complicated since finite mass effects at $\mathcal{O}(\alpha_s)$ differ for vector and axial-vector current induced jet production,

$$\frac{d\hat{\sigma}_b^{\text{ns}}}{d\tau} = e^{-2\frac{\delta(R,\mu_s)}{Q}\frac{\partial}{\partial\tau}}\Big[\sigma_0^{bv} f_b^v\Big(\tau, \frac{\bar{m}_b}{Q}, \frac{\mu_{\text{ns}}}{Q}\Big)$$

$$+\,\sigma_0^{ba} f_b^a\Big(\tau, \frac{\bar{m}_b}{Q}, \frac{\mu_{\text{ns}}}{Q}\Big)\Big]$$

$$+\,(\overline{\text{MS}}\text{-pole mass scheme change terms})\,. \qquad (46)$$

In our analysis we implement analytic expressions for the nonsingular functions f_b^v and f_b^a. The full $\mathcal{O}(\alpha_s)$ distributions for $\tau > 0$ can be obtained from integrating the known double differential $b\bar{b}$ energy distribution for vector-induced and axial-vector-induced production, respectively, see e.g. Refs. [76, 77].[9] The corresponding $\mathcal{O}(\alpha_s)$ coefficient of the $\delta(\tau - \tau_b^{\min})$ term is obtained using the one-loop correction to the total $b\bar{b}$ cross section as a constraint. To determine the nonsingular distributions $f_b^{v,a}$ we proceed much like for the massless case and subtract the singular contributions expanded to $\mathcal{O}(\alpha_s)$ from the full $\mathcal{O}(\alpha_s)$ distribution. Further details and explicit formulas for $f_b^{v,a}$ will be given in a future publication.

H. QED Corrections

For the electroweak corrections to the thrust distribution we can distinguish purely weak contributions and QED effects. The dominant effects to jet production from the purely weak interactions are given by virtual one-loop corrections to the hard Wilson coefficient H_Q. Since the contribution of the singular thrust distribution $d\hat{\sigma}_s/d\tau$ dominates in the τ ranges we use for our fits as well as in the total cross section $\sigma_{\text{tot}} = \int d\tau\,d\sigma/d\tau$ (see Fig. 7), the purely weak corrections largely drop out when the distribution is normalized to the total cross section. This is consistent with the explicit computations carried out in Refs. [43, 44], where purely weak corrections were found to be tiny. In our analysis we therefore neglect purely weak effects.

---

[9] Results for bottom mass corrections at $\mathcal{O}(\alpha_s^2)$ were determined in Refs. [78, 79, 80], but are not used in our analysis due to the small effect the bottom mass corrections have in our fits.

For QED corrections the situation is more complicated because, apart from virtual effects which again largely cancel in the normalized distribution, one also has corrections due to initial state and final state radiation. In addition, one has to account for the fact that the treatment of QED effects in the thrust measurements depends on the experiment. In general, using Monte Carlo simulations, all experimental data were corrected to eliminate the effects from initial state radiation. However, they differ concerning the treatment of final state photon corrections, which were either eliminated or included in the corrected data sets. In Sec. VI we review information on the approach followed by the various experimental collaborations. Since many experiments did not remove final state radiation, we have configured a version of our code that adds final state photons and QED Sudakov effects, and does so on an experiment by experiment basis. A parametric estimate of the potential impact of these QED effects on the measurement of $\alpha_s(m_Z)$ is $\sim -0.244\,\alpha_{\rm em}/(C_F\alpha_s) \sim -1\%$, where 0.244 is the average of the square of the electromagnetic charges for the five lightest flavors.

We implement the leading set of QED corrections to all components that go into the main factorization formula of Eq. (4) in the massless quark limit counting $\alpha_{\rm em} \sim \alpha_s^2$ to make a correspondence with Tab. II and remembering to include cross terms such as terms of $\mathcal{O}(\alpha_{\rm em}\alpha_s)$. Exceptions where QED corrections are not included are the gap subtraction $\delta(R,\mu_S)$ and the R-evolution equation for the gap parameter $\bar{\Delta}$. This is because QED effects do not lead to $\mathcal{O}(\Lambda_{\rm QCD})$ infrared renormalon ambiguities. Most of the required QED results can be obtained in a straightforward manner from modifications of the known QCD corrections.

Our implementation of QED effects is briefly described as follows: For the evolution of the strong coupling we included the $\mathcal{O}(\alpha_s^2\alpha_{\rm ew})$ corrections to the QCD beta function. There are also effects from the evolution of the QED coupling $\alpha_{\rm em}(\mu)$ which we define in the $\overline{\rm MS}$ scheme. In the beta function for the QED coupling $\alpha_{\rm em}$ we account for the dominant $\mathcal{O}(\alpha_{\rm em}^2)$ and the next-to-leading $\mathcal{O}(\alpha_{\rm em}^2\alpha_s)$ contributions. For the full singular partonic distribution which includes both QCD and QED effects we have

$$\frac{{\rm d}\hat{\sigma}_{\rm s}}{{\rm d}\tau} = Q \sum_I \sigma_0^I \, H_Q^I(Q,\mu_H)\, U_H^I(Q,\mu_H,\mu)\!\int\! {\rm d}s\, {\rm d}s'$$
$$\times J_\tau^I(s',\mu_J)\, U_J^{\tau I}(s-s',\mu,\mu_J) \int\! {\rm d}k\, U_S^{\tau I}(k,\mu,\mu_S)$$
$$\times e^{-2\frac{\delta(R,\mu_S)}{Q}\frac{\partial}{\partial\tau}}\, S_\tau^{{\rm part}I}\Big(Q\,\tau - \frac{s}{Q} - k,\mu_S\Big), \qquad (47)$$

where all factors now depend on the index I due to their dependence on the electromagnetic charges $q^{I=uv,ua} = +2/3$ and $q^{I=dv,da,bv,ba} = -1/3$. We implement one-loop QED corrections in the hard factor H_Q^I, the jet function J_τ^I and the soft functions $S_\tau^{{\rm part}I}$. In the renormalization group evolution factors U_H^I, $U_J^{\tau I}$, $U_S^{\tau I}$ we account for the one-loop QED corrections to the cusp and the non-cusp anomalous dimensions. In the nonsingular partonic distribution ${\rm d}\hat{\sigma}_{\rm ns}/{\rm d}\tau$ the same approach is employed. Here the $\mathcal{O}(\alpha_{\rm em})$ contributions that are analogous to the $\mathcal{O}(\alpha_s)$ terms are included by writing the full functions f^I to be used in Eq. (26) as

$$f^I\Big(\tau,\frac{\mu_{\rm ns}}{Q}\Big) = f_{\rm qcd}^I\Big(\tau,\frac{\mu_{\rm ns}}{Q}\Big) + \frac{3\,\alpha(\mu)\,(q^I)^2}{8\pi} f_1(\tau). \quad (48)$$

The 1% parametric estimate and the moderate size of the QED effects we observe from the results of our fits justifies the neglect of higher order QED effects. A more precise treatment of QED effects is also not warranted given the level of accuracy of the Monte Carlo generators used to correct the experimental data. More details and explicit formulae for the QED corrections discussed here will be given in a future publication.

III. PROFILE FUNCTIONS

The factorization formula for the singular partonic distribution ${\rm d}\hat{\sigma}_{\rm s}/{\rm d}\tau$ in Eq. (11) is governed by three renormalization scales, the hard scale μ_H, the jet scale μ_J, and the soft scale μ_S. To avoid large logarithms appearing in the corrections to the hard coefficient H_Q, the jet function J_τ and the soft function S_τ, the corresponding scales must satisfy the following theoretical constraints in the three τ regions:

1) peak: $\mu_H \sim Q\,,\ \ \mu_J \sim \sqrt{\Lambda_{\rm QCD}Q}\,,\ \ \ \mu_S \gtrsim \Lambda_{\rm QCD}\,,$
2) tail: $\mu_H \sim Q\,,\ \ \mu_J \sim Q\sqrt{\tau}\,,\ \ \ \ \ \ \mu_S \sim Q\tau\,,$
3) far-tail: $\mu_H = \mu_J = \mu_S \sim Q\,.$ (49)

In the peak region, where the full nonperturbative function $S_\tau^{\rm mod}$ is relevant we have $\mu_H \gg \mu_J \gg \mu_S \sim \Lambda_{\rm QCD}$. In the tail region, where the nonperturbative effects are described by a series of moments of the soft function we have $\mu_H \gg \mu_J \gg \mu_S \gg \Lambda_{\rm QCD}$. To achieve an accurate theoretical description, we resum logarithms of τ in the peak and tail region where μ_H, μ_J, and μ_S are separated. Finally, in the far-tail region the partonic contributions are described by usual fixed-order perturbation theory, and a proper treatment of fixed order multijet thresholds requires that the three μ parameters merge close together in the far-tail region and become equal at $\tau = 0.5$, with $\mu_H = \mu_J = \mu_S \sim Q \gg \Lambda_{\rm QCD}$. Thus in the far-tail region logarithms of τ are not summed. The merging of μ_H, μ_J, and μ_S in the far-tail region is of key importance for the cancellations between singular and nonsingular cross sections shown in Fig. 7. To obtain a continuous factorization formula that is applicable in all three regions we use τ-dependent renormalization scales, which we call *profile functions*. These are smooth functions of τ which satisfy the theoretical constraints listed in Eq. (49).

In addition to the three renormalization scales of the singular partonic distribution there are two more scales, $\mu_{\rm ns}$ and R. The renormalization scale $\mu_{\rm ns}$ governs the

perturbative series for the function f^I contained in the nonsingular partonic distribution $d\hat{\sigma}_{\rm ns}/d\tau$. The subtraction scale R arises when we implement the gap subtractions in the R-gap scheme for Ω_1 that remove the $\mathcal{O}(\Lambda_{\rm QCD})$ renormalon contained in the $\overline{\rm MS}$ soft function. This R also corresponds to the endpoint of the R-evolution for $\bar{\Delta}(R, \mu_S)$ given in Eq. (41). To avoid large logarithms in the subtraction $\delta(R, \mu_S)$, the value of R needs to be chosen of order μ_S and is therefore also a function of τ.

The factorization formula (4) is formally invariant under $\mathcal{O}(1)$ changes of the profile function scales, that is, changes that do not modify the hierarchies. The residual dependence on the choice of profile functions constitutes one part of the theoretical uncertainties and provides a method to estimate higher order perturbative corrections. We adopt a set of six parameters that can be varied in our theory error analysis which encode this residual freedom while still satisfying the constraints in Eq. (49).

For the profile function at the hard scale, we adopt

$$\mu_H = e_H\, Q, \tag{50}$$

where e_H is a free parameter which we vary from $1/2$ to 2 in our theory error analysis.

For the soft profile function we use the form

$$\mu_S(\tau) = \begin{cases} \mu_0 + \frac{b}{2t_1}\tau^2, & 0 \le \tau \le t_1, \\ b\,\tau + d, & t_1 \le \tau \le t_2, \\ \mu_H - \frac{b}{1-2t_2}(\frac{1}{2}-\tau)^2, & t_2 \le \tau \le \frac{1}{2}. \end{cases} \tag{51}$$

Here, t_1 and t_2 represent the borders between the peak, tail and far-tail regions. μ_0 is the value of μ_S at $\tau = 0$. Since the thrust value where the peak region ends and the tail region begins is Q dependent, we define the Q-independent parameter $n_1 = t_1\,(Q/1\,{\rm GeV})$. To ensure that $\mu_S(\tau)$ is a smooth function, the quadratic and linear forms are joined by demanding continuity of the function and its first derivative at $\tau = t_1$ and $\tau = t_2$, which fixes $b = 2\left(\mu_H - \mu_0\right)/\left(t_2 - t_1 + \frac{1}{2}\right)$ and $d = \left[\mu_0(t_2 + \frac{1}{2}) - \mu_H t_1\right]/\left(t_2 - t_1 + \frac{1}{2}\right)$. In our theory error analysis we vary the free parameters n_1, t_2 and μ_0.

The profile function for the jet scale is determined by the natural relation between the hard, jet, and soft scales

$$\mu_J(\tau) = \left(1 + e_J\left(\frac{1}{2} - \tau\right)^2\right)\sqrt{\mu_H\,\mu_S(\tau)}. \tag{52}$$

The term involving the free $\mathcal{O}(1)$-parameter e_J implements a modification to this relation and vanishes in the multijet region where $\tau = 1/2$. We use a variation of e_J to include the effect of such modifications in our estimation of the theoretical uncertainties.

For the subtraction scale R the choice $R = \mu_S(\tau)$ ensures that we avoid large logarithms in the $\delta_i(R, \mu_S)$ subtractions for the soft function. In the peak region, however, it is convenient to deviate from this choice so that the $\mathcal{O}(\alpha_s)$ subtraction term $\delta_1(R, \mu_S) =$
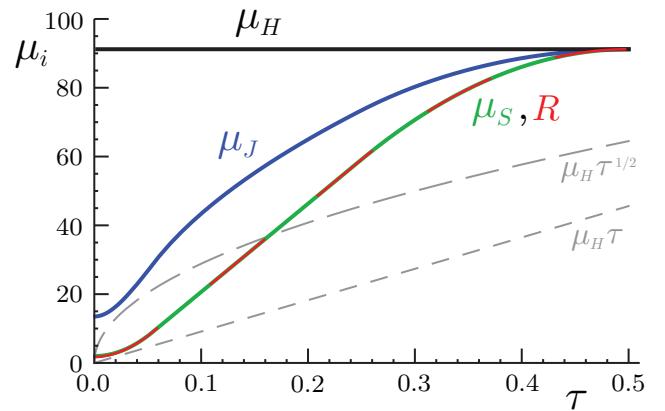

FIG. 8: Profile functions for the renormalization scales $\mu_J(\tau)$, $\mu_S(\tau)$, and subtraction scale $R(\tau)$ that appear in the factorization theorem. Shown are results for the central parameter values at $Q = m_Z$.

$-0.848826\,\ln(\mu_S/R)$ is nonzero (see Eq. (38)). We therefore use the form

$$R(\tau) = \begin{cases} R_0 + \mu_1\,\tau + \mu_2\tau^2, & 0 \le \tau \le t_1, \\ \mu_S(\tau), & t_1 \le \tau \le 0.5\,. \end{cases} \tag{53}$$

Imposing continuity of $R(\tau)$ and its first derivative at $\tau = t_1$ requires $\mu_1 = (2d - 2R_0 + b\,t_1)/t_1$ and $\mu_2 = (-d + R_0)/t_1^2$. The only free parameter is R_0 which sets the value of R at $\tau = 0$. We take $R_0 = 0.85\mu_0$ to give the one loop subtraction $\delta_1(R, \mu_S)$ the appropriate sign to cancel the renormalon in the peak region. Since our focus here is not the peak region, we leave further discussion of the appropriate choice of R_0 to a future publication.

In our theory error analysis we vary $\mu_{\rm ns}$ to account for our ignorance on the resummation of logarithms of τ in the nonsingular corrections. We account for the possibilities

$$\mu_{\rm ns}(\tau) = \begin{cases} \mu_H, & n_s = 1, \\ \mu_J(\tau), & n_s = 0, \\ \frac{1}{2}(\mu_J(\tau) + \mu_S(\tau)), & n_s = -1. \end{cases} \tag{54}$$

We do not include the choice $\mu_{\rm ns} = \mu_S$ since we find that the choice of this small scale enhances the nonsingular contributions in an unnatural way.

In total, we have introduced six free parameters which we vary to account for renormalization scale uncertainties. In our analysis we use the following central values and variations: $\mu_0 = 2^{+0.5}_{-0.5}$ GeV, $n_1 = 5^{+3}_{-3}$, $t_2 = 0.25^{+0.05}_{-0.05}$, $e_J = 0^{+1}_{-1}$, $e_H = 2^h$ with $h = 0^{+1}_{-1}$ and $n_s = (-1, 0, 1)$. In Fig. 8 we show the form of the profile functions for $Q = m_Z = 91.2$ GeV and all profile parameters at their central values. The dashed lines represent the functions $Q\sqrt{\tau}$ and $Q\tau$ which were the central choices for $\mu_J(\tau)$ and $\mu_S(\tau)$ used in Ref. [20], but which do not meet in the multijet region. In order for our profile for

$\mu_S(\tau)$ to join smoothly onto μ_H and $\mu_J(\tau)$ it is necessary for $\mu_S(\tau)$ to have a slope $\sim 2Q\tau$ in the tail region. Since $\ln 2$ is not large our profiles sum the same $\ln\tau$'s as with the choice in Ref. [20], but satisfy the criteria necessary to treat the multijet thresholds.[10]

IV. NONPERTURBATIVE MODEL FUNCTION

The soft nonperturbative function $S_\tau^{\mathrm{mod}}(k)$ parameterizes the dominant nonperturbative hadronic effects in the thrust distribution. It describes the hadronization contributions that arise from how soft hadrons that are radiated in between the jets enter the thrust variable in Eq. (1). It is normalized, has the property $S_\tau(0) = 0$, is positive definite and has support for $k \geq 0$. To keep the representation of S_τ^{mod} as much as possible independent of a particular analytic parametrization we adopt the approach of Ref. [38] and write the soft nonperturbative function as a linear combination of an infinite set of basis functions which can in principle describe any function with the properties mentioned above. The model function we use has the form

$$S_\tau^{\mathrm{mod}}(k,\lambda,\{c_i\}) = \frac{1}{\lambda}\left[\sum_{n=0}^{N} c_n\, f_n\!\left(\frac{k}{\lambda}\right)\right]^2, \quad (55)$$

where the basis functions are [38]

$$f_n(z) = 8\sqrt{\frac{2z^3(2n+1)}{3}}\; e^{-2z}\, P_n\!\big(g(z)\big),$$

$$g(z) = \frac{2}{3}\Big(3 - e^{-4z}\left(3 + 12z + 24z^2 + 32z^3\right)\Big) - 1, \quad (56)$$

and P_n are Legendre polynomials. For $\sum_i c_i^2 = 1$ the norm of $S_\tau^{\mathrm{mod}}(k)$ is unity, $\Omega_0 = 1$. The choice of basis in Eqs. (55) and (56) depends on specifying one dimensionful parameter λ which is characteristic of the width of the soft function. With $N = \infty$ the parameter λ would be redundant, but in practice we truncate the sum in Eq. (55) at a finite N, and then λ is effectively an additional parameter of the model function.

In this work we fit to experimental thrust data in the tail region where the predominant effects of the soft model function are described by its first moment $\Omega_1(\lambda,\bar\Delta,\{c_i\})$. As explained below, we use the second moment $\Omega_2(\lambda,\bar\delta,\{c_i\})$ to validate our error analysis and confirm the validity of neglecting this parameter in the fit. Since in the tail region the exact form of the soft model function is not relevant, we take $N = 2$ setting $c_{n>2} = 0$. Variations of the parameter c_1 are highly correlated with variations of λ and are hence not necessary

for our purposes, so we set $c_1 = 0$. For this case

$$\Omega_1 = \bar\Delta + \frac{\lambda}{2}\left[c_0^2 + 0.201354 c_0 c_2 + 1.10031 c_2^2\right],$$

$$\Omega_2 = \bar\Delta^2 + \bar\Delta\lambda\left[c_0^2 + 0.201354 c_0 c_2 + 1.10031 c_2^2\right]$$

$$+ \frac{\lambda^2}{4}\left[1.25 c_0^2 + 1.03621 c_0 c_2 + 1.78859 c_2^2\right], \quad (57)$$

and the normalization condition $c_0^2 + c_2^2 = 1$ can be used to eliminate $c_0 > 0$. Recall that in the soft model function in the factorization theorem we must use $S_\tau^{\mathrm{mod}}\big(k - 2\bar\Delta(R,\mu_S),\lambda,\{c_i\}\big)$ where $R = R(\tau)$ and $\mu_S = \mu_S(\tau)$ are determined by the profile functions. When we quote numbers for parameters we use $\bar\Delta = \bar\Delta(R_\Delta,\mu_\Delta)$ and hence $\Omega_{1,2} = \Omega_{1,2}(R_\Delta,\mu_\Delta)$ with reference scales $\mu_\Delta = R_\Delta = 2\,\mathrm{GeV}$. The running between the scales (R,μ_S) and (R_Δ,μ_Δ) is determined by Eq. (41).

For our default fit in the tail region only the parameter Ω_1 is numerically relevant so without loss of generality we can take $c_0 = 1$, $c_2 = 0$, and set $\bar\Delta(R_\Delta,\mu_\Delta) = 0.05$ GeV. In this case all higher moments $\Omega_{n>1}$ are determined as a function of Ω_1 and $\bar\Delta$. For example we have $\Omega_2 = (\bar\Delta^2 - 2\bar\Delta\Omega_1 + 5\Omega_1^2)/4$ for the second moment.

In Sec. VII we analyze the dependence of our fit results on changes of Ω_2. Because c_2 has a rather strong correlation to Ω_2, we implement these Ω_2 variations by using Eq. (57) and setting c_2 to nonzero values. In this case we can hold Ω_1 fixed by a suitable choice of λ for a given c_2.

To obtain results from our code that do not include nonperturbative corrections we can simply turn them off by setting $S_\tau^{\mathrm{mod}}(k) = \delta(k)$ and $\bar\Delta = \delta = 0$.

V. NORMALIZATION AND CONVERGENCE

The experimental data is normalized to the total number of events. In our prediction we therefore need to normalize the distribution to the total cross section, i.e. we have to calculate $(1/\sigma)\mathrm{d}\sigma/\mathrm{d}\tau$. Since the factorization formula in Eq. (4) is valid for all thrust values we have the option to use either the integral of our $\mathrm{d}\sigma/\mathrm{d}\tau$ distribution for the norm, or the available fixed-order result for the total hadronic cross section.

The fixed-order total cross section is

$$\sigma_{\mathrm{tot}}^{\mathrm{FO}} = \sum \sigma_0^I R^I, \quad R^{uv} = R^{dv} = R^{ua} = R^{da} = R_{\mathrm{Had}},$$

$$R^{ba} = R_{\mathrm{Had}} + R_A + \frac{\alpha_s^2}{3\pi^2} I(r_t), \quad R^{bv} = R_{\mathrm{Had}} + R_V.$$

$$(58)$$

Here R_{Had} is the pure QCD cross section for massless quarks, $R_{A,V}$ are mass corrections depending on m_b/Q, and $I(r_t)$ is the isosinglet correction from the axial anomaly and large top-bottom mass splitting [56]. Setting $\mu = Q$ the QCD cross sections for massless quarks at three loops is

$$R_{\mathrm{Had}} = 1 + 0.3183099\,\alpha_s(Q) + 0.1427849\,\alpha_s^2(Q)$$

---

[10] In Ref. [23] where NLL resummation is achieved by exponentiation, the log resummation is turned off at a predefined threshold τ_{max} with the log-R method [21]. In this approach the transition to fixed order results in the multijet region differs from ours.

$$- 0.411757\,\alpha_s^3(Q)\,. \tag{59}$$

We refer to the review in Ref. [81] for a discussion of the fixed-order hadronic cross section. We note that the α_s series for the fixed-order hadronic cross section exhibits an excellent and fast convergence. At $\mathcal{O}(\alpha_s^3)$ the perturbative uncertainty is much below the permille level and hence entirely negligible for the purpose of our analysis.

In the R-gap scheme in pure QCD, from a numerical analysis at $Q = m_Z$, we find at $\mathrm{N^3LL'}$ order that the integrated norm of the thrust distribution for the default setting of all theory parameters (see Tab. III) gives about $0.99\,\sigma_{\mathrm{tot}}^{\mathrm{FO}}$ at $\mathcal{O}(\alpha_s^3)$. However we also find that the perturbative uncertainty of the integrated norm (determined by the theory scan as described in Sec. VI) is about $\pm 2.5\%$, which is substantially larger than for the fixed-order cross section. This larger uncertainty is due to the perturbative errors of the thrust distribution in the peak region. At $\mathrm{N^3LL'}$ order we therefore employ the fixed order cross section to normalize the thrust distribution we use for the fits.

At the lower orders in the R-gap scheme ($\mathrm{N^3LL}$, $\mathrm{NNLL'}$, NNLL, $\mathrm{NLL'}$) we find that the integrated norm for central theory parameters is more appropriate since the order-by-order convergence to $\sigma_{\mathrm{tot}}^{\mathrm{FO}}$ is substantially slower than that of the rapid converging fixed-order QCD result in Eq. (59). Again we find that the large perturbative uncertainties in the peak region render the perturbative errors of the integrated norm larger than those of the fixed-order norm. We therefore evaluate the integrated norms at the lower orders with the theory parameters fixed at their default values (see Tab. III). This means that to estimate the theoretical errors in our fits to experimental data at orders below $\mathrm{N^3LL'}$ in the R-gap scheme, we vary the theory parameters only for the distribution and not for the norm computation. In the $\overline{\mathrm{MS}}$ scheme for $\bar{\Omega}_1$ we also adopt the integrated norm at all orders. When we evaluate the thrust distribution with log-resummation but without nonperturbative effects we use the same normalization choices as for the R-gap scheme, which makes comparison to earlier work in Sec. IX easier. For the situation where the cross-section is evaluated at fixed-order, without resummation or nonperturbative effects, we use the appropriate fixed order normalization at each order.

As discussed in Sec. VI, to compare with the binned experimental data we integrate our theoretical expression for the distribution $(1/\sigma)(d\sigma/d\tau)$ over each bin $[\tau_1, \tau_2]$. A potential alternative is to use theoretical results for the cumulant

$$\Sigma(\tau) = \int_0^\tau d\tau'\,\frac{1}{\sigma}\frac{d\sigma}{d\tau}(\tau')\,. \tag{60}$$

Here one sums large logs of τ rather than τ', and the SCET based cumulant has τ dependent profiles, $\Sigma(\tau, \mu_i(\tau))$. The presence of $\mu_i(\tau)$ implies that the derivative of the cumulant is not precisely equal to the distribution,

$$\frac{d}{d\tau}\Sigma\big(\tau, \mu_i(\tau)\big) = \frac{1}{\sigma}\frac{d\sigma}{d\tau}\big(\tau, \mu_i(\tau)\big) \tag{61}$$

$$+ \frac{d\mu_i(\tau)}{d\tau}\frac{\partial}{\partial\mu_i}\int_0^\tau d\tau'\,\frac{d\sigma}{d\tau'}\big(\tau', \mu_i(\tau)\big)\,.$$

The difference coming from the second term in Eq. (61) can be numerically important for certain observables. To test this we consider using for the cross-section integrated over the bin $[\tau_1, \tau_2]$ the theoretical expression

$$\Sigma(\tau_2, \mu_i(\tilde{\tau}_2)) - \Sigma(\tau_1, \mu_i(\tilde{\tau}_1))\,, \tag{62}$$

and will examine several choices for $\tilde{\tau}_{1,2}$.

One simple possibility is to use $\tilde{\tau}_1 = \tau_1$ and $\tilde{\tau}_2 = \tau_2$, so that $\Sigma(\tau_2, \mu_i(\tau_2)) - \Sigma(\tau_1, \mu_i(\tau_1))$ is used. In this case there is a spurious contribution from outside the $[\tau_1, \tau_2]$ bin associated to the second term in Eq. (61),

$$\Sigma(\tau_1, \mu_i(\tau_2)) - \Sigma(\tau_1, \mu_i(\tau_1)) \tag{63}$$
$$\simeq (\tau_2 - \tau_1)\frac{d\mu_i(\tau_1)}{d\tau}\frac{\partial}{\partial\mu_i}\int_0^{\tau_1} d\tau'\,\frac{d\sigma}{d\tau'}\big(\tau', \mu_i(\tau_1)\big)\,,$$

where the $\simeq$ holds under the approximation that the derivative do not change very much across the bin. With our default setup the deviation of this simple choice for the cumulants from our integrated result for the distribution is 2% to 8% for $\tau \in [0.1, 0.3]$, bin-size $\tau_2 - \tau_1 = 0.01$, and $Q = 91.2\,\mathrm{GeV}$.[11] In the far-tail region $\tau_1 \in [0.3, 0.45]$, where the cross-section becomes small, the deviation grows from 8% to 1000%. These deviations are dominated by the spurious contribution. The size of the spurious contribution is not reduced by increasing the bin-size to $\tau_2 - \tau_1 = 0.05$, and is only mildly dependent on Q. Any choice in Eq. (62) where $\tilde{\tau}_1 \neq \tilde{\tau}_2$ leads to a spurious contribution from $\tau \in [0, \tau_1]$.

If we instead use $\tilde{\tau}_1 = \tilde{\tau}_2 = (\tau_1 + \tau_2)/2$ then the spurious contribution is identically zero. In this case the difference between Eq. (62) and our integrated thrust distribution is reduced to 0.5% for $\tau_1 \in [0.1, 0.3]$ and for $\tau_1 \in [0.3, 0.45]$ grows from 0.5% to only 20%. Although dramatically reduced, the difference to the integrated distribution in the far-tail region is still quite sizeable. This discrepancy occurs because only for the distribution $(1/\sigma)(d\sigma/d\tau)$ can the $\mu_i(\tau)$ profile functions be constructed such that they satisfy exactly the criteria discussed in Sec. III. Due to the above issues, and since the binned datasets are intended as representations of the thrust distribution, we have determined that our approach of integrating the thrust distribution is conceptually the best.

In the rest of this section we discuss the perturbative behavior of the thrust distribution in the tail region. The values of the physical parameters used in our numerical analysis are collected in Eq. (A4). For our lower order fits we always use the four-loop beta function in the running of the strong coupling constant, as mentioned in the

---

[11] For the profile functions used by Becher and Schwartz [20], discussed in section IX, this deviation has similar size but opposite sign.
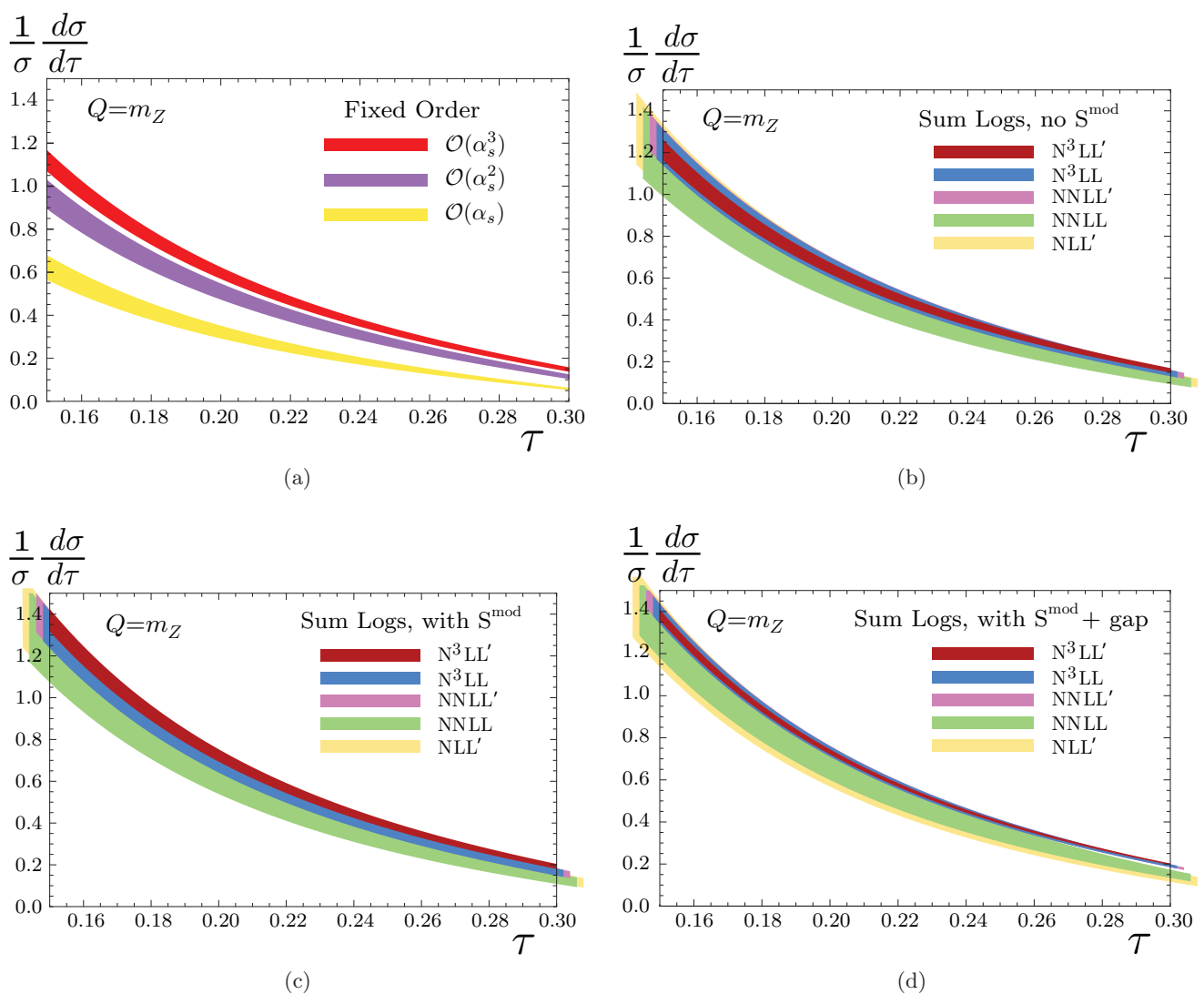
FIG. 9: Theory scan for errors in pure QCD with massless quarks. The panels are a) fixed-order, b) resummation with no nonperturbative function, c) resummation with a nonperturbative function using the $\overline{\rm MS}$ scheme for $\bar{\Omega}_1$ without renormalon subtraction, d) resummation with a nonperturbative function using the R-gap scheme for Ω_1 with renormalon subtraction.

caption of Tab. II. Furthermore, we always consider five active flavors in the running and do not implement bottom threshold corrections, since our lowest scale in the profile functions (the soft scale μ_S) is never smaller than 6 GeV in the tail where we perform our fit.

In Fig. 9 we display the normalized thrust distribution in the tail thrust range $0.15 < \tau < 0.30$ at the different orders taking $\alpha_s(m_Z) = 0.114$ and $\Omega_1(R_\Delta, \mu_\Delta) = 0.35\,{\rm GeV}$ as reference values, and neglecting m_b and QED corrections. We display the case $Q = m_Z$ where the experimental measurements from LEP-I have the smallest statistical uncertainties. The qualitative behavior of the results agrees with other c.m. energies. The colored bands represent the theoretical errors of the predictions at the respective orders, which have been determined by the scan method described in Sec. VI.

In Fig. 9a we show the $\mathcal{O}(\alpha_s)$ (light/yellow), $\mathcal{O}(\alpha_s^2)$

(medium/purple) and $\mathcal{O}(\alpha_s^3)$ (dark/red) fixed-order thrust distributions without summation of large logarithms. The common renormalization scale is chosen to be the hard scale μ_H. In the fixed-order results the higher order corrections are quite large and our error estimation obviously underestimates the theoretical uncertainty of the fixed-order predictions. This panel including the error bands is very similar to the analogous figures in Refs. [4] and [6]. This emphasizes the importance of summing large logarithms.

In Fig. 9b the fully resummed thrust distributions at NLL' (yellow), NNLL (green), NNLL' (purple), N³LL (blue) and N³LL' (red) order are shown, but without implementing the soft nonperturbative function $S_\tau^{\rm mod}$ or the renormalon subtractions related to the R-gap scheme. The yellow NLL' error band is mostly covered by the green NNLL order band, and similarly the purple NNLL'

band is covered by the blue N^3LL one. Moreover the blue N^3LL band is within the purple NNLL band. Compared to the fixed-order results, the improvement coming from the systematic summation of large logarithms is obvious. In particular we see that our way of estimating theoretical uncertainties is appropriate once the logarithms are properly summed. At N^3LL and at N^3LL' order the relative uncertainties of these resummed thrust distributions in the tail region $\tau \in [0.1, 0.3]$ are about $\pm 7.8\%$ and $\pm 4.6\%$, respectively.

The results shown in Fig. 9c are very similar to panel b but now include also the soft nonperturbative function S_τ^{mod} without renormalon subtractions, where $\bar{\Omega}_1$ is defined in the $\overline{\mathrm{MS}}$ scheme. In the tail region the soft nonperturbative function leads to a horizontal shift of the distribution towards larger thrust values by an amount $\delta\tau \propto 2\bar{\Omega}_1/Q$. This is clearly visible by comparing the values at $\tau = 0.15$ where the curves intersect the y-axis. Concerning the uncertainty bands and the behavior of predictions at the different orders the results are very similar to those in panel b.

Finally, in Fig. 9d we show the results with summation of large logarithms including the soft model function with renormalon subtractions, where Ω_1 is defined in the R-gap scheme. In the R-gap scheme the convergence of perturbation theory is improved, and correspondingly the size of the uncertainties from the same variation of the theory parameters is decreased. The decrease of the uncertainties is clearly visible comparing the blue N^3LL and the red N^3LL' uncertainty bands with panel c. The relative uncertainties of the thrust distribution at N^3LL and at N^3LL' order in the tail region $\tau \in [0.1, 0.3]$ are now about $\pm 3.4\%$ and $\pm 1.7\%$, respectively. This improvement illustrates the numerical impact of the $\mathcal{O}(\Lambda_{\mathrm{QCD}})$ renormalon contained in the partonic soft function and shows the importance of eliminating the $\mathcal{O}(\Lambda_{\mathrm{QCD}})$ renormalon.

VI. EXPERIMENTAL DATA AND FIT PROCEDURE

Experimental data for thrust are available for various c.m. energies Q between 14 and 207 GeV. In our analysis we fit the factorization formula (4) in the tail region to extract α_s and Ω_1. As our default data set we use the thrust range $6/Q \leq \tau \leq 0.33$, and we only employ data from $Q \geq 35$ GeV. The lower boundary $6/Q$ removes data in the peak where higher order moments become important, while the upper boundary of 0.33 removes data in the far-tail region where the $\alpha_s\Lambda_{\mathrm{QCD}}/Q$ power corrections become more important. We take $Q \geq 35$ GeV since a more sophisticated treatment of b quark effects is required at lower energies. The data we use are from TASSO with $Q = \{35, 44\}$ GeV [82], AMY with $Q = 55.2$ GeV [83], JADE with $Q = \{35, 44\}$ GeV [84], SLC with $Q = 91.2$ GeV [85], L3 with $Q = \{41.4, 55.3, 65.4, 75.7, 82.3, 85.1, 91.2, 130.1, 136.1, 161.3, 172.3,$

$182.8, 188.6, 194.4, 200.0, 206.2\}$ GeV [72, 86], DELPHI with $Q = \{45, 66, 76, 89.5, 91.2, 93, 133, 161, 172, 183, 189, 192, 196, 200, 202, 205, 207\}$ GeV [87, 88, 89, 90], OPAL with $Q = \{91, 133, 161, 172, 177, 183, 189, 197\}$ GeV [91, 92, 93] and ALEPH with $Q = \{91.2, 133, 161, 172, 183, 189, 200, 206\}$ GeV [94]. (For TASSO and AMY we have separated statistical and systematic errors using information from the experimental papers.) All data is given in binned form, and we therefore integrate Eq. (4) over the same set of bins to obtain appropriate theory results for the fit to the experimental numbers. For the case that either $\tau = 6/Q$ or $\tau = 0.33$ are located within an experimental bin, that bin is excluded from the data set if more than half of it lies outside the chosen interval. For the $Q > m_Z$ data we removed five bins with downward fluctuations that were incompatible at the > 10-sigma level with the cross section implied by neighboring data points and other experimental data in the same region. The list of these bins is: L3 (136.1 GeV): $[0.25, 0.275]$, DELPHI (161 GeV): $[0.32, 0.40]$, DELPHI (183 GeV): $[0.08, 0.09]$, DELPHI (196 GeV): $[0.16, 0.18]$, ALEPH (200 GeV): $[0.16, 0.20]$.[12] Our default global data set contains a total of 487 bins. In the numerical analysis performed in Sec. VII we also examine alternative global data sets with different τ-ranges.

The data sets were corrected by the experiments to eliminate the QED effects from initial state radiation using bin-by-bin correction factors determined from Monte Carlo simulations. The primary aim of these corrections was to eliminate the effective reduction of the c.m. energy available for the production of the hadronic final state. In addition, in the data sets from the TASSO, L3 and ALEPH collaborations the effects from final state radiation of photons were eliminated, while they have been fully included in the data sets from the AMY, JADE, SLC, DELPHI and OPAL collaborations. It should also be noted that the approaches used by the experiments to treat photon radiation were dependent on the c.m. energy Q. For the $Q = m_Z$ data any radiation of initial state photons is naturally suppressed as the effective c.m. energy for the hadronic final state gets shifted away from the Z pole. Therefore no specific photon cuts were applied for the $Q = m_Z$ data prior to the application of the bin-by-bin correction factors. For the data taken off the Z pole for either $Q < m_Z$ or $Q > m_Z$ the effects of initial state radiation are substantial and explicit hard photon cuts were applied in the data taking prior to the application of the bin-by-bin correction procedure. We therefore consider the $Q = m_Z$ data sets as more reliable concerning the treatment of QED effects.

Since the size of the QED effects we find in the mea-

---

[12] Four out of these bins lie in our $\tau \in [6/Q, 0.33]$ default fit range. If they are included in the default dataset then for our final fit in Eq. (68) the $\chi^2 = 439$ increases by $+81$ and the central fit values show a slight decrease to $\alpha_s(m_Z) = 0.1132$ and a slight increase to $\Omega_1 = 0.336$ GeV.

parameter	default value	range of values
μ_0	$2\,\mathrm{GeV}$	1.5 to 2.5 GeV
n_1	5	2 to 8
t_2	0.25	0.20 to 0.30
e_J	0	-1,0,1
e_H	1	0.5 to 2.0
n_s	0	-1,0,1
s_2	-39.1	-36.6 to -41.6
Γ_3^{cusp}	1553.06	-1553.06 to $+4569.18$
j_3	0	-3000 to $+3000$
s_3	0	-500 to $+500$
ϵ_2	0	-1,0,1
ϵ_3	0	-1,0,1

TABLE III: Theory parameters relevant for estimating the theory uncertainty, their default values and range of values used for the theory scan during the fit procedure.

surements of α_s and the soft function moment Ω_1 is comparable to the experimental uncertainties (see the results and discussions in Sec. VII), a less Monte Carlo dependent treatment of QED radiation would be certainly warranted. (See Ref. [44] for a recent discussion of QED radiation based on full one-loop matrix elements.) However, given that the impact of QED corrections we find for α_s and Ω_1 is still smaller than the current theoretical uncertainties from QCD, we use for our default numerical analysis the theory code with QED effects switched on, as described in Sec. II H. In Sec. VII we also present results when QED corrections are neglected for all data sets, and for the case when they are neglected only for the TASSO, L3 and ALEPH data sets.

For the fitting procedure we use a χ^2-analysis, where we combine the statistical and the systematic experimental errors into the correlation matrix. We treat the statistical errors of all bins as independent. The systematic errors of the bins are correlated, but - unfortunately - practically no information on the correlation is given in the experimental publications. We therefore have to rely on a correlation model. For our analysis we assume as the default that within one thrust data set, i.e. for the set of thrust bins obtained by one experiment at one Q value, the systematic experimental errors are correlated in the minimal overlap model used by the LEP QCD working group [91, 94]. In the minimal overlap model the off-diagonal entries of the experimental covariance matrix for the bins i and j within one data set are equal to $[\min(\Delta_i^{\mathrm{sys}}, \Delta_j^{\mathrm{sys}})]^2$, where $\Delta_{i,j}^{\mathrm{sys}}$ are the systematic errors of the bins i and j. This model implies a positive correlation of systematic uncertainties within each thrust data set. As a cross check that our default correlation model does not introduce a strong bias we also carry out fits were the experimental systematic errors are assumed to be uncorrelated. Details are given in Sec. VII.

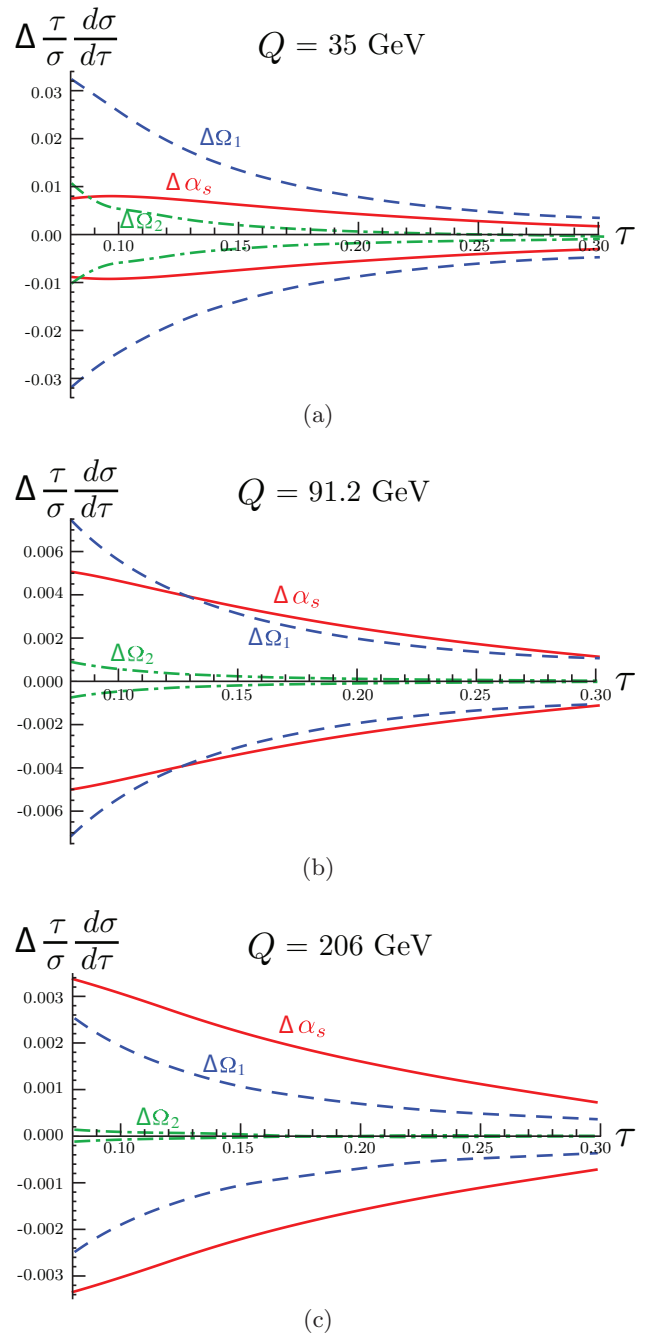To estimate the theoretical errors in the α_s-Ω_1 plane at

(a)

(b)

(c)

FIG. 10: Difference between default cross section and the cross section varying only one parameter as a function of τ. We vary $\alpha_s(m_Z)$ by ± 0.001 (solid red curves), $2\Omega_1$ by ± 0.1 (dashed blue curves) and c_2 by ± 0.5 (dash dotted green curves). The plot is shown for three different values of the center of mass energy: (a) $Q = 35\,\mathrm{GeV}$, (b) $Q = 91.2\,\mathrm{GeV}$, (c) $Q = 206\,\mathrm{GeV}$.

any order and for any approximation used for the factorization formula (4), we carry out independent fits for 500 different sets of theory parameters which are randomly chosen in the ranges discussed in the previous sections and summarized in Tab. III. We take the area covered

by the points of the best fits in the α_s-Ω_1 plane as the theory uncertainty treated like 1-sigma.[13] We emphasize that this method to estimate theoretical errors is more conservative than the error band method [26] employed for example in Refs. [20, 22]. However, our method required considerably more computer power and it was necessary to use the Tier-2 centers at Garching and MIT, as well as clusters at the MPI and the University of Arizona. In Sec. VII we also present the outcome of other ways to estimate the theoretical error.

It is an important element of our analysis that we carry out global fits to the data from all values of $Q \geq 35$ (and all experiments). This is motivated by the strong degeneracy between α_s and Ω_1 in the tail region which can only be lifted when data from different Q values are simultaneously included in the fits.[14] In Fig. 10 the difference $\mathrm{d}\sigma/\mathrm{d}\tau - (\mathrm{d}\sigma/\mathrm{d}\tau)_{\mathrm{default}}$ is displayed for $0.08 \leq \tau \leq 0.30$ and $Q = 35$, 91.2 and 206 GeV. Here $(\mathrm{d}\sigma/\mathrm{d}\tau)_{\mathrm{default}}$ is the cross section for the default setting of the theory parameters with $\alpha_s(m_Z) = 0.114$ and $\Omega_1 = 0.35\,\mathrm{GeV}$ and for $\mathrm{d}\sigma/\mathrm{d}\tau$ we vary either $\alpha_s(m_Z)$ by ± 0.001 (solid red curves) or $2\Omega_1$ by $\pm 0.1\,\mathrm{GeV}$ (dashed blue curves) from their default values. The figures show that in the tail region changes in α_s can be compensated by changes in Ω_1. This degeneracy makes it impossible to determine α_s and Ω_1 simultaneously with small uncertainties from tail fits that use data from one Q value (or from a narrow range of Q values). On the other hand, we see that the correlation is Q dependent when considering a large enough range of Q values. In our fits it is particularly important to include, apart from the data from $Q = m_Z$, the low-energy data from JADE, TASSO, and AMY, and the high energy data from the LEP-II experiments. Although the errors in these analyses are larger than from the high-statistics $Q = m_Z$ run at LEP-I these data sets are essential for breaking the degeneracy and simultaneously extracting α_s and Ω_1.

VII. NUMERICAL ANALYSIS

Having explained all ingredients of the factorization formula (4) and the fit procedure we are now in the position to discuss the numerical results of our analysis based on a global fit to the experimental data for $Q \geq 35$ GeV in the tail region. In the tail region the dominant power corrections are encoded in the first moment Ω_1, see Eq. (6), so we can determine $\alpha_s(m_Z)$ and Ω_1 from a simultaneous fit. In this section we examine in detail the numerical results of our fits concerning the treatment of the pertur-

---

order	$\alpha_s(m_Z)$ (with $\bar\Omega_1^{\overline{\mathrm{MS}}}$)	$\alpha_s(m_Z)$ (with Ω_1^{Rgap})
NLL'	0.1203 ± 0.0079	0.1191 ± 0.0089
NNLL	0.1222 ± 0.0097	0.1192 ± 0.0060
NNLL'	0.1161 ± 0.0038	0.1143 ± 0.0022
N^{3}LL	0.1165 ± 0.0046	0.1143 ± 0.0022
N^{3}LL' (full)	0.1146 ± 0.0021	$\mathbf{0.1135 \pm 0.0009}$
N^{3}LL'$_{(\mathrm{QCD}+m_b)}$	0.1153 ± 0.0022	0.1141 ± 0.0009
N^{3}LL'$_{(\mathrm{pure\ QCD})}$	0.1152 ± 0.0021	0.1140 ± 0.0008

TABLE IV: Theory errors from the parameter scan and central values for $\alpha_s(m_Z)$ at various orders. The N^{3}LL' value above the horizontal line is our final scan result, while the N^{3}LL' values below the horizontal line show the effect of leaving out the QED corrections, and leaving out both the b-mass and QED respectively. The central values are the average of the maximal and minimal values reached from the scan.

order	$\bar\Omega_1$ ($\overline{\mathrm{MS}}$)	Ω_1 (R-gap)
NLL'	0.264 ± 0.213	0.293 ± 0.203
NNLL	0.256 ± 0.197	0.276 ± 0.155
NNLL'	0.283 ± 0.097	0.316 ± 0.072
N^{3}LL	0.274 ± 0.098	0.313 ± 0.071
N^{3}LL' (full)	0.252 ± 0.069	$\mathbf{0.323 \pm 0.045}$
N^{3}LL'$_{(\mathrm{QCD}+m_b)}$	0.238 ± 0.070	0.310 ± 0.049
N^{3}LL'$_{(\mathrm{pure\ QCD})}$	0.254 ± 0.070	0.332 ± 0.045

TABLE V: Theory errors from the parameter scan and central values for Ω_1 defined at the reference scales $R_\Delta = \mu_\Delta = 2$ GeV in units of GeV at various orders. The N^{3}LL' value above the horizontal line is our final scan result, while the N^{3}LL' values below the horizontal line show the effect of leaving out the QED corrections, and leaving out both the b-mass and QED respectively. The central values are the average of the maximal and minimal values reached from the scan.

bative, hadronization and experimental errors, QED and bottom mass corrections and their dependence on the choice of the data set. We note that the values quoted for Ω_1 in the R-gap scheme are given for reference scales $R_\Delta = \mu_\Delta = 2$ GeV, see Sec. II F.

Theory Scan

In Fig. 11 the best fit points of the theory parameters scan in the α_s-$2\Omega_1$ plane are displayed at NLL' (brown), NNLL (magenta), NNLL' (green), N^{3}LL (blue) and N^{3}LL' (red) order. The fit results at N^{3}LL' order include bottom mass and QED corrections. In Fig. 11a the results in the R-gap scheme with renormalon subtractions are shown, and in Fig. 11b the results in the $\overline{\mathrm{MS}}$ scheme without gap subtractions are given.

At each order 500 fits were carried out with the theory parameters randomly chosen in the ranges given in Tab. III. As described in Sec. VI, we take the size of the area in the α_s-$2\Omega_1$ plane covered by the best fit points as a measure for the theoretical uncertainties. To visualize the theoretical uncertainties we have colored the
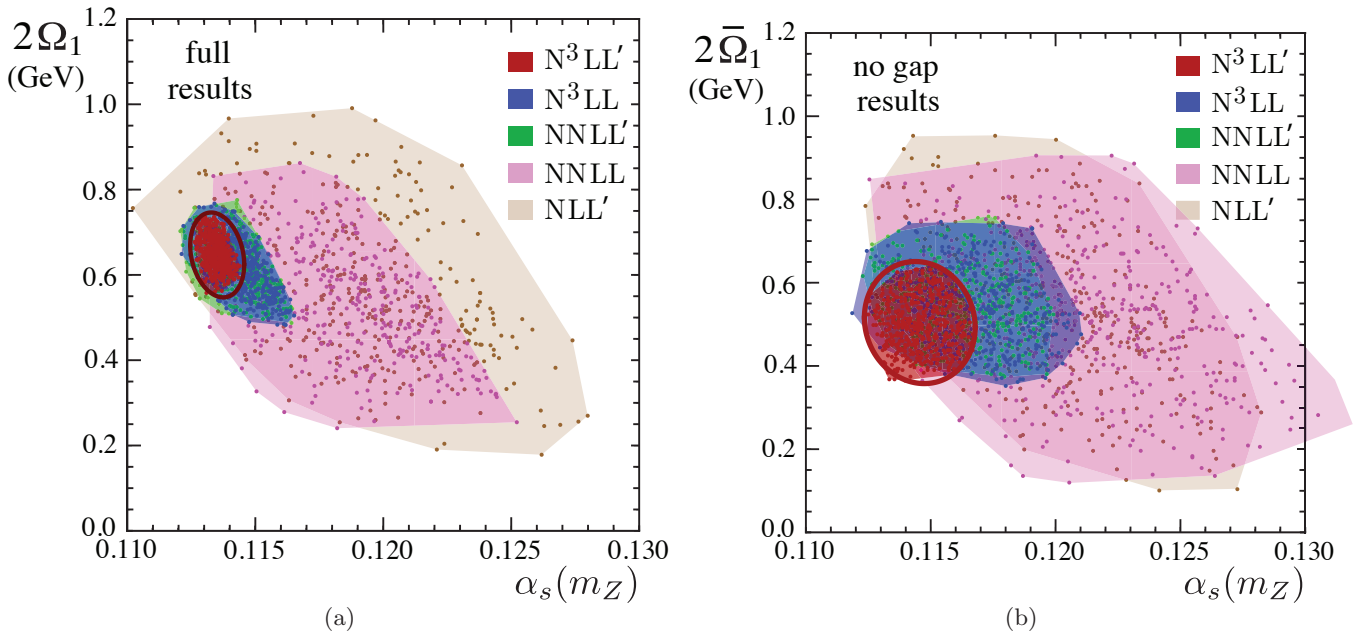
FIG. 11: Distribution of best fit points in the $\alpha_s(m_Z)$-$2\Omega_1$ and $\alpha_s(m_Z)$-$2\bar{\Omega}_1$ planes. Panel (a) shows results including pertur-bation theory, resummation of the logs, the soft nonperturbative function and Ω_1 defined in the R-gap scheme with renormalon subtractions. Panel (b) shows the results as in panel a, but with $\bar{\Omega}_1$ defined in the $\overline{\text{MS}}$ scheme without renormalon subtractions. In both panels the respective total (experimental+theoretical) 39% CL standard error ellipses are displayed (thick dark red lines), which correspond to 1-sigma (68% CL) for either one-dimensional projection.
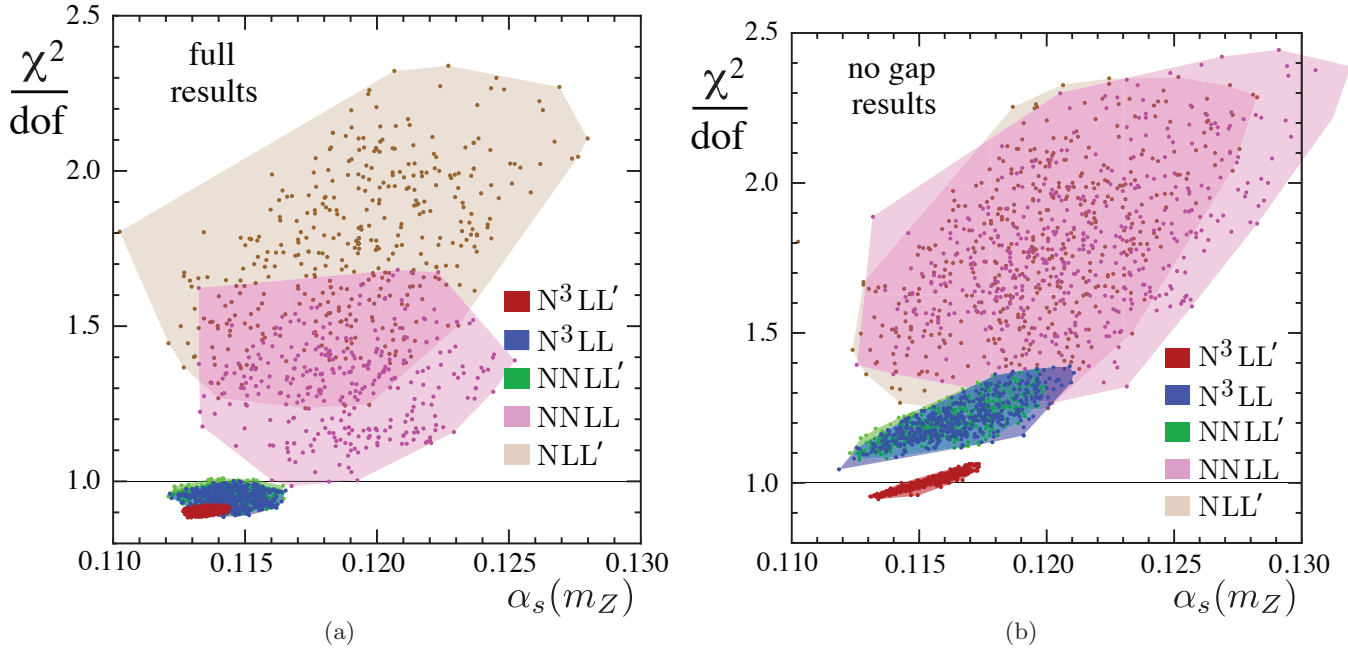

FIG. 12: Distribution of best fit points in the $\alpha_s(m_Z)$-χ^2/dof plane. Panel (a) shows the χ^2/dof values of the points given in Fig. 11a. Panel (b) shows the χ^2/dof values of the points given in Fig. 11b.

respective areas according to the orders. The fit results clearly show a substantial reduction of the theoretical uncertainties with increasing orders. Explicit numerical results for the respective central values (determined by the mean of the respective maximal and minimal values) and the theory errors (determined by half of the difference between maximal and minimal values) for α_s and Ω_1 are given in Tabs. IV and V, respectively. We will consider these theory errors as 1-sigma. At N³LL′ order with Ω_1 in the R-gap scheme the theory error for

$$\frac{\tau}{\sigma}\frac{d\sigma}{d\tau}$$

Fit at N^{3}LL$'$ for $\alpha_s(m_Z)$ & Ω_1

theory scan error
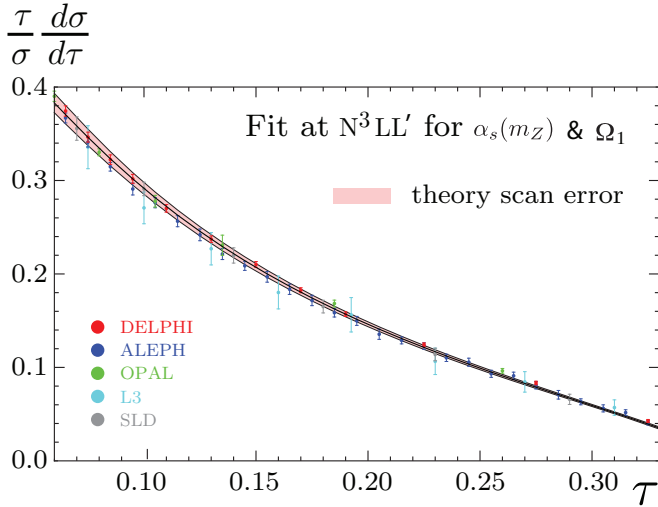
● DELPHI
● ALEPH
● OPAL
● L3
● SLD

FIG. 13: Thrust distribution at N^{3}LL$'$ order and $Q = m_Z$ including QED and m_b corrections using the best fit values for $\alpha_s(m_Z)$ and Ω_1 in the R-gap scheme given in Eq. (68). The pink band represents the perturbative error determined from the scan method described in Sec. VI. Data from DELPHI, ALEPH, OPAL, L3, and SLD are also shown.

$\alpha_s(m_Z)$ is ± 0.0009 compared to ± 0.0021 with $\bar{\Omega}_1$ in the $\overline{\text{MS}}$ scheme. Also at NNLL$'$ and N^{3}LL we see that the removal of the $\mathcal{O}(\Lambda_{\text{QCD}})$ renormalon leads to a reduction of the theoretical uncertainties by about a factor of two in comparison to the results with $\bar{\Omega}_1$ in the $\overline{\text{MS}}$ scheme without renormalon subtraction. The proper treatment of the renormalon subtraction is thus a substantial part of a high-precision analysis for Ω_1 as well as for α_s.

It is instructive to analyze the minimal χ^2 values for the best fit points shown in Fig. 11. In Fig. 12 the distributions of the best fits in the α_s-χ^2_{min}/dof plane are shown using the color scheme of Fig. 11. Figure 12a displays the results in R-gap scheme, and Fig. 12b the ones in the $\overline{\text{MS}}$ scheme. For both schemes we find that the χ^2_{min} values and the size of the covered area in the α_s-χ^2_{min}/dof plane systematically decrease with increasing order. While the analysis in the $\overline{\text{MS}}$ scheme for $\bar{\Omega}_1$ leads to χ^2_{min}/dof values around unity and thus an adequate description of the entire global data set at N^{3}LL$'$ order, we see that accounting for the renormalon subtraction in the R-gap scheme leads to a substantially improved theoretical description having χ^2_{min}/dof values below unity already at NNLL$'$ and N^{3}LL orders, with the N^{3}LL$'$ order result slightly lower at χ^2_{min}/dof $\simeq 0.91$. This demonstrates the excellent description of the experimental data contained in our global data set. It also validates the smaller theoretical uncertainties we obtain for α_s and Ω_1 at N^{3}LL$'$ order in the R-gap scheme.

As an illustration of the accuracy of the fit, in Fig. 13 we show the theory thrust distributions at $Q = m_Z$ for the full N^{3}LL$'$ order with the R-gap scheme for Ω_1, for the default theory parameters and the corresponding best fit values shown in bold in Tabs. IV and V. The pink

	Band method 1	Band method 2	Our scan method
N^{3}LL$'$ with Ω_1^{Rgap}	0.0004	0.0008	0.0009
N^{3}LL$'$ with $\bar{\Omega}_1^{\overline{\text{MS}}}$	0.0016	0.0019	0.0021
N^{3}LL$'$ without S_τ^{mod}	0.0018	0.0021	0.0034
$\mathcal{O}(\alpha_s^3)$ fixed-order	0.0018	0.0026	0.0046

TABLE VI: Theoretical uncertainties for $\alpha_s(m_Z)$ obtained at N^{3}LL$'$ order from two versions of the error band method, and from our theory scan method. The uncertainties in the R-gap scheme (first line) include renormalon subtractions, while the ones in the $\overline{\text{MS}}$ scheme (second line) do not and are therefore larger. The same uncertainties are obtained in the analysis without nonperturbative function (third line). Larger uncertainties are obtained from a pure $\mathcal{O}(\alpha_s^3)$ fixed-order analysis (lowest line). Our theory scan method is more conservative than the error band method.

band displays the theoretical uncertainty from the scan method. The fit result is shown in comparison with data from DELPHI, ALEPH, OPAL, L3, and SLD, and agrees very well. (Note that the theory values displayed are actually binned according to the ALEPH data set and then joined by a smooth interpolation.)

Band Method

It is useful to compare our scan method to determine the perturbative errors with the error band method [26] that was employed in the analyses of Refs. [20, 22, 25]. In the error band method first each theory parameter is varied separately in the respective ranges specified in Tab. III while the rest are kept fixed at their default values. The resulting envelope of all these separate variations with the fit parameters $\alpha_s(m_Z)$ and Ω_1 held at their best fit values determines the error bands for the thrust distribution at the different Q values. Then, the perturbative error is determined by varying $\alpha_s(m_Z)$ keeping all theory parameters to their default values and the value of the moment Ω_1 to its best fit value. The resulting perturbative errors of $\alpha_s(m_Z)$ for our full N^{3}LL$'$ analysis in the R-gap scheme are given in the first line of Tab. VI. In the second line the corresponding errors for $\alpha_s(m_Z)$ in the $\overline{\text{MS}}$ scheme for $\bar{\Omega}_1$ are displayed. The left column gives the error when the band method is applied such that the $\alpha_s(m_Z)$ variation leads to curves strictly inside the error bands for all Q values. For this method it turns out that the band for the highest Q value is the most restrictive and sets the size of the error. The resulting error for the N^{3}LL$'$ analysis in the R-gap scheme is more than a factor of two smaller than the error obtained from our theory scan method, which is shown in the right column. Since the high Q data has a much lower statistical weight than the data from $Q = m_Z$, we do not consider this method to be sufficiently conservative and conclude that it should not be used. The middle column gives the perturbative error when the band method is applied such that the $\alpha_s(m_Z)$ variation minimizes a χ^2 function which